



HAL
open science

Establishing 20S Proteasome Genetic, Translational and Post-Translational Status from Precious Biological and Patient Samples with Top-Down MS

Angelique Sanchez Dafun, Dušan Živković, Stephen Adonai Leon-Icaza, Sophie Möller, Carine Froment, Delphine Bonnet, Adriana Almeida de Jesus, Laurent Alric, Muriel Quaranta-Nicaise, Audrey Ferrand, et al.

► To cite this version:

Angelique Sanchez Dafun, Dušan Živković, Stephen Adonai Leon-Icaza, Sophie Möller, Carine Froment, et al.. Establishing 20S Proteasome Genetic, Translational and Post-Translational Status from Precious Biological and Patient Samples with Top-Down MS. *Cells*, 2023, 12 (6), pp.844. 10.3390/cells12060844 . hal-04159042

HAL Id: hal-04159042

<https://hal.inrae.fr/hal-04159042v1>

Submitted on 11 Jul 2023

HAL is a multi-disciplinary open access archive for the deposit and dissemination of scientific research documents, whether they are published or not. The documents may come from teaching and research institutions in France or abroad, or from public or private research centers.











L'archive ouverte pluridisciplinaire **HAL**, est destinée au dépôt et à la diffusion de documents scientifiques de niveau recherche, publiés ou non, émanant des établissements d'enseignement et de recherche français ou étrangers, des laboratoires publics ou privés.



Distributed under a Creative Commons Attribution 4.0 International License

Article

Establishing 20S Proteasome Genetic, Translational and Post-Translational Status from Precious Biological and Patient Samples with Top-Down MS

Angelique Sanchez Dafun ¹, Dušan Živković ¹, Stephen Adonai Leon-Icaza ¹, Sophie Möller ², Carine Froment ¹, Delphine Bonnet ^{3,4}, Adriana Almeida de Jesus ⁵, Laurent Alric ⁴, Muriel Quaranta-Nicaise ³, Audrey Ferrand ³, Céline Cougoule ¹, Etienne Meunier ¹, Odile Burlet-Schiltz ¹, Frédéric Ebstein ^{2,†}, Raphaëla Goldbach-Mansky ⁵, Elke Krüger ², Marie-Pierre Bousquet ^{1,*} and Julien Marcoux ^{1,*}

¹ Institut de Pharmacologie et de Biologie Structurale (IPBS), Université de Toulouse, CNRS, Université Toulouse III—Paul Sabatier (UPS), 31077 Toulouse, France

² Institute of Medical Biochemistry and Molecular Biology, University Medicine Greifswald, 17475 Greifswald, Germany

³ IRSD, Université de Toulouse, INSERM, INRAE, ENVT, Université de Toulouse III—Paul Sabatier (UPS), 31300 Toulouse, France

⁴ Internal Medicine Department of Digestive Disease, Rangueil Hospital, Université de Toulouse III—Paul Sabatier (UPS), 31400 Toulouse, France

⁵ Translational Autoinflammatory Diseases Section, LCIM, National Institute of Allergy and Infectious Diseases, National Institutes of Health, Bethesda, MD 20892, USA

* Correspondence: marie.pierre-bousquet@ipbs.fr (M.-P.B.); julien.marcoux@ipbs.fr (J.M.)

† Present address: L'institut du Thorax, Nantes Université, Inserm UMR 1087/CNRS UMR 6291, 44000 Nantes, France.



Citation: Dafun, A.S.; Živković, D.; Leon-Icaza, S.A.; Möller, S.; Froment, C.; Bonnet, D.; de Jesus, A.A.; Alric, L.; Quaranta-Nicaise, M.; Ferrand, A.; et al. Establishing 20S Proteasome Genetic, Translational and Post-Translational Status from Precious Biological and Patient Samples with Top-Down MS. *Cells* **2023**, *12*, 844. <https://doi.org/10.3390/cells12060844>

Academic Editors: Marcus Groettrup and Michael Basler

Received: 5 December 2022

Revised: 23 February 2023

Accepted: 27 February 2023

Published: 8 March 2023



Copyright: © 2023 by the authors. Licensee MDPI, Basel, Switzerland. This article is an open access article distributed under the terms and conditions of the Creative Commons Attribution (CC BY) license (<https://creativecommons.org/licenses/by/4.0/>).

Abstract: The mammalian 20S catalytic core of the proteasome is made of 14 different subunits (α 1-7 and β 1-7) but exists as different subtypes depending on the cell type. In immune cells, for instance, constitutive catalytic proteasome subunits can be replaced by the so-called immuno-catalytic subunits, giving rise to the immunoproteasome. Proteasome activity is also altered by post-translational modifications (PTMs) and by genetic variants. Immunochemical methods are commonly used to investigate these PTMs whereby protein-tagging is necessary to monitor their effect on 20S assembly. Here, we present a new miniaturized workflow combining top-down and bottom-up mass spectrometry of immunopurified 20S proteasomes that analyze the proteasome assembly status as well as the full proteoform footprint, revealing PTMs, mutations, single nucleotide polymorphisms (SNPs) and induction of immune-subunits in different biological samples, including organoids, biopsies and B-lymphoblastoid cell lines derived from patients with proteasome-associated autoinflammatory syndromes (PRAAS). We emphasize the benefits of using top-down mass spectrometry in preserving the endogenous conformation of protein modifications, while enabling a rapid turnaround (1 h run) and ensuring high sensitivity (1–2 pmol) and demonstrate its capacity to semi-quantify constitutive and immune proteasome subunits.

Keywords: immunoproteasome; PRAAS; proteasome; proteoform; top-down proteomics; label-free quantification

1. Introduction

During evolution, the constitutive catalytic proteasome subunits (c20S) β 1/ β 2/ β 5 gave rise to the catalytic immunoproteasome (i20S) subunits β 1i/ β 2i/ β 5i [1]. Intermediate forms also exist, in which only one or two constitutive catalytic subunits are replaced [2]. The incorporation of these alternative immunoproteasome isoforms, which share ~60–70% sequence identity with their standard counterparts, modulates proteasome

activity, regulator binding, substrate specificity and the amino acid sequence of the peptides generated [3–7]. We recently showed that substitutions occurring in the core particle subunits lead to conformational changes that alter the 20S interactome and function [8,9]. The i20S and its intermediates are constitutively expressed in immune cells, however, their expression can be induced in almost any tissue by proinflammatory stimuli [10]. In infected tissues, it can replace up to 90% of the c20S [11]. The peptides generated by the i20S may serve as epitopes, presented by Major Histocompatibility Complex (MHC) class I molecules at the cell surface. T lymphocytes use these MHC class I/peptide complexes to differentiate healthy from abnormal or infected cells. A peptide recruited into the MHC-class I complex must fulfill two prerequisites: an appropriate length of 8–9 amino acid residues and certain C-terminal anchor residues, which are basic or hydrophobic in humans. The replacement of standard subunits by immunosubunits alters the peptide profile generated by proteasomes: the resulting peptides have C-termini that are not acidic and more hydrophobic, resulting in a greater number of successfully presented antigens [12]. One role of the i20S is thus to modulate the MHC class I antigen presentation in cases of infection or transformation, thereby improving the immune response. Beyond antigen presentation, the i20S is essential in maintaining the proliferation of T cells in response to infection [13] and oxidative stress [14–16] or in maintaining protein homeostasis upon cytokine signaling or in immune cells [17–20].

Post-translational modifications (PTMs) or mutations in proteasome subunits and activators can alter proteasome activity. PTMs by phosphorylation, methylation, acetylation, ubiquitination and myristoylation have been linked to either increases or decreases in proteasome activity; however, their precise role in proteasome function still needs to be elucidated (reviewed in refs. [21,22]). Pathologies including cancers, heart diseases, neurological diseases, type 2 diabetes, inflammatory bowel disease (IBD) and proteasome-associated autoinflammatory syndromes (PRAAS), to name a few, have also been directly linked to the altered activity of the proteasome (reviewed in refs. [23–26]). PRAAS span the disease spectrum, ranging from chronic atypical neutrophilic dermatosis with lipodystrophy and elevated temperature (CANDLE) to joint contractures, muscle atrophy, microcytic anemia and panniculitis-induced lipodystrophy (JMP), Nakajo-Nishimura syndrome (NNS) and Japanese autoinflammatory syndrome with lipodystrophy (JASL), which are autoinflammatory syndromes mainly caused by genetic mutations in the immunoproteasome subunit $\beta 5i$ (encoded by *PSMB8*) [18,27–33]. Previous publications in PRAAS also reported mutations in $\beta 1i$ (*PSMB9*) [34], and $\beta 2i$ (*PSMB10*) [35]; compound heterozygous mutations in the constitutive subunit $\beta 7$ (*PSMB4*) [18,36]; digenic mutations in $\beta 5i$ and constitutive subunit- $\alpha 7$ (*PSMA3*) or $\beta 7$ (*PSMB4*), and in $\beta 1i$ and $\beta 7$ [18]; and mutations in the 20S chaperones PAC2 and POMP [18,37,38]. More recently, mutations in the subunits of the 19S (the major 20S regulator) RPN5 (*PSMD12*) or RPT5 (*PSMC3*) have been linked to neurodevelopmental disorders [39–41].

The proteasome has also been the target for drug development. Three proteasome inhibitors targeting its chymotrypsin-like activity have been approved by the FDA since 2003 for the treatment of multiple myeloma [42–44]. However, a better understanding of proteasome regulation would allow more specific therapies targeting specific proteasome subtypes, thus avoiding unnecessary shutdown of downstream pathways that may cause off-target side-effects [43–45]. The group of Marcus Groettrup showed that specific inhibition of the i20S reduces graft rejection [46] and suppresses the progression of colorectal cancer in mice [47], but recent results have shown that targeting a single catalytic subunit of the i20S was not sufficient to achieve efficient therapeutic goals [45]. In this regard, quantifying the relative abundance of the i20S vs. c20S proteasome within a sample/cell extract or biopsy is of paramount importance.

To date, most groups working on proteasome function have assessed and investigated the i20S proteasome, PTMs and proteasome mutations by Western blot (WB) using specific antibodies [18,48,49]. Although very sensitive and compatible with complex samples (typically cell lysates), WB has limitations including cross-reactivity of certain

antibodies, slower throughput, and poor quantitation capacities, and the method hardly provides valuable information regarding the nature and relative abundances of the detected proteoforms, which can include mature forms as well as truncated, proteolyzed, variant and/or modified isoforms. In addition, epitope tagging of mutant and wild-type (WT) constructs is often necessary to monitor PTMs and the impact of disease-causing mutations [18,49]. Our lab developed a series of mass spectrometry (MS)-based bottom-up (BU) proteomics methods aimed at detecting and quantifying proteasome subunits, including two-dimensional gel electrophoresis and isotope-coded affinity tag (ICAT) labeling [50], label-free proteomics [51,52], protein correlation profiling [5], stable isotope labeling by amino acids in cell culture (SILAC)-based multiplexed LC-selected reaction monitoring (SRM) [15], and more recently, top-down (TD) proteomics [8,9].

The latter consists of analyzing entire protein, rather than trypsin-digested proteins, as is commonly the case in BU proteomics, with the advantage of directly obtaining the accurate molecular weights (MW) of the proteins, and hence their potential combination(s) of PTMs, putative truncations and/or mutations and single nucleotide polymorphisms (SNPs) [53]. Furthermore, sequence coverage is usually pretty low in BU proteomics, and proteins are commonly identified and quantified based only on a small subset as low as one to three peptides; the BU database search only finds PTMs and mutations if these were previously included in database and searched for, and it is required that the peptides have the correct size and charge. The main current limitation of TD proteomics resides in the fact that proteins of different MW can have very different ionization yields, with smaller proteins usually displaying better “flyability”. It is commonly accepted that proteins <30 kDa are easily amenable to TD proteomics [54], which is ideal for the 20S proteasome, since all the α and β subunits have a MW between 20–30 kDa. The other advantage of TD proteomics is that the proteoform footprint can be relatively quickly obtained (~2 h including data analysis) and requires minimal amounts of proteins (~1–5 pmol), making it a convenient solution for quality control assessment and in-depth subunit characterization. We and others have already successfully applied this technique to 20S from commercial sources [8,55] or immunopurified from HEK cells expressing either the c20S or i20S [8]. More recently, we used TD proteomics to characterize the proteoforms of the spermatoproteasome immunopurified from bovine testes and muscle [9]. Beyond the identification and characterization of proteoforms, TD proteomics represents a novel avenue for protein quantification or semi-quantification (for a detailed review see [56]). Briefly, TD quantification methods are either based on metabolic labeling (i.e., SILAC [57]), isobaric chemical labeling (i.e., tandem mass tag [58,59]) or on label-free [54,60–62] approaches; each method has its pros and cons. Label-free quantification has the advantage of being less expensive and can be applied to any sample in theory (no need to use labelled media or feedstock), but multiplexing is not possible, and the method can arguably be less reproducible and sensitive. As mentioned before, differences in ionization yields can be challenging for label-free quantification, and this becomes even more evident in TD than in BU proteomics. Directly comparing the intensities of identical proteoforms in different samples/runs, an approach called “differential TD”, is a way to circumvent this problem [61].

In this work, we set out to develop a rapid TD-MS method to establish the proteoforms of 20S proteasome subunits and to gain information on their PTMs, mutations related to PRAAS and more common SNPs and immuno subunits on IFN γ -induced Caco2 cells, lung organoid and intestinal crypts. We also investigated the use of relative signal intensity for label-free quantification of the different subunits. Our approach consists of semi-quantifying the different 20S proteoforms within the same sample/run, which is quite different from differential TD. We first established relative ionization yields (RIY) for each standard and immunosubunit, using HEK EBNA cells producing either pure c20S or pure i20S [5,8]. We then applied this method to monitor the i20S induction by IFN γ in Caco2 cells and then to semi-quantify c20S vs. i20S in lung organoids and intestinal crypts.

2. Materials & Methods

2.1. Reagents

All reagents were provided by Sigma-Aldrich-Merck (St. Louis, MO, USA) unless otherwise specified. Substrates for activity assay (Suc-LLVY-AMC, Boc-LRR-AMC, and Z-LLE-AMC) were purchased from Enzo Life Science (Farmingdale, NY, USA). The protein quantity was estimated using the DC Protein Assay from Bio-Rad (Hercules, CA, USA).

2.2. Cell Lines, Organoids and Crypts

2.2.1. HEK293-EBNA Cells

Human HEK293-EBNA cells expressing only either c20S or i20S, as previously described in ref. [2], were grown in Iscove's Modified Dulbecco's Medium (IMDM) supplemented with 10% fetal bovine serum (FBS), 116 mg/L L-Arginine and 36 mg/L L-Asparagine. For cells expressing i20S, the medium was also supplemented with 5 µg/mL puromycin and 600 µg/mL hygromycin B to maintain selective pressure. All cultures were supplemented with 100 units/ml penicillin, 100 µg/ml streptomycin, and maintained at 37 °C under 5% CO₂. The medium was replaced every 2–3 days, and cell passaging was carried out at around 80% confluence. The cells were washed with Dulbecco's phosphate-buffered saline (DPBS) three times and stored at –80 °C until use.

2.2.2. Caco2 Cells

Caco2 cells were grown in Dulbecco's Modified Eagle Medium (DMEM) Glutamax high glucose (4.5 g/L) plus pyruvate with 20% FBS. All cultures were supplemented with 100 units/ml penicillin, 100 µg/mL streptomycin, and maintained at 37 °C under 5% CO₂. The medium was replaced every 2–3 days and cell passaging was carried out at around 70% confluence.

2.2.3. B lymphoblastoid Cells

Immortalized B lymphoblastoid cell lines (BLCL) were generated from three PRAAS patients: A (β5i T75M homozygous), B (β5i T75M and α7 R233del), and C (β7 D212_V214del and β7 5'UTR c.-9G>A) as well as from the parents of Patient C, who are both clinically healthy but have β7 D212_V214del and β7 5'UTR c.-9G>A mutations, respectively. Cell lines were also generated from four other unrelated healthy controls. BLCL were cultured and amplified in RPMI 1640 medium supplemented with 10% FBS and 1% penicillin/streptomycin. Cells were washed twice with PBS and subsequently snap-frozen in liquid nitrogen.

2.2.4. Airway Organoids

Healthy airway organoids were derived from human lung biopsies of healthy adjacent tissue from patients with lung cancer, as previously reported, and maintained in complete culture media [63,64]. On day 30 of culture, nine drops (each containing ~20 organoids) of 40 µL Cultrex growth factor reduced BME type 2 (Trevigen) previously seeded on a 24-well plate (Nunclon Delta surface, Thermo Scientific, San Jose, CA, USA) were washed twice with cold 1X phosphate-buffered saline (PBS). Each drop was harvested in 500 µL of 1X PBS and pooled in a 15 mL Falcon tube before centrifugation (800× g for 5 min). After centrifugation, the supernatant was discarded, and the pellet was resuspended in 2 mL of cold cell recovery solution (Corning) and kept at 4 °C for 20 min. Finally, organoids were centrifuged at 800× g for 5 min, and the pellet was washed twice with cold 1X PBS.

2.2.5. Intestinal Crypts

Colonic samples were obtained from either surgical resections of a patient suffering from colorectal cancer or from a patient displaying a low-grade pseudoperitoneal myxoma of appendicular origin (Table 1). Crypts were harvested in healthy zones of the colon. Crypts extracted from the second patient were harvested at the margin of the resection, and at least 10 cm away from the tumor. 15,000 and 50,000 crypts were extracted from

these patients, respectively, corresponding to ~1 mg and ~3 mg of total protein in their corresponding lysates, according to our protein DC assay. The patients' characteristics were as follows:

Table 1. Characteristics of patients from which colonic samples were obtained.

Age (Years)	Sex	Medical Status
66	M	Low-grade pseudoperitoneal myxoma of appendicular origin
59	M	Suspicion of colorectal cancer

2.3. Caco2 Cells Treatment with Different Proinflammatory Cytokines

In 6-well plates (Nunclon Delta surface, Thermo Scientific), Caco2 cells (seeding density: 8000 cells/cm³; in triplicates) were treated with different cytokines, namely 10 ng/mL interferon- γ (IFN γ), 100 ng/mL tumor necrosis factor- α (TNF- α), 100 ng/mL interleukin-6 (IL-6), 100 ng/mL interleukin-1 β (IL-1 β), or 10 μ g/mL lipopolysaccharide (LPS), for three days. After washing the cells with DPBS three times, 0.5 mL of 5% SDS in 50 mM ammonium bicarbonate pH 7.6 was added per well, then the cells were scraped and transferred into 2 mL tubes. Tubes were stored at -80°C until use.

2.4. Caco2 Cells Treatment with IFN γ

In a 150 mm Petri-dish (Nunc EasYDish, Thermo Scientific), Caco2 cells (seeding density: 8000 cells/cm³) were treated with 10 ng/mL IFN γ (PeproTech, Rocky Hill, NJ, USA) for 3, 7, and 11 days. The cells were washed with DPBS three times and stored at -80°C until use.

2.5. Purification of c20S and i20S from HEK293-EBNA Cell Lines

Large scale purification of proteasomes was carried out using MCP21 antibody grafted in cyanogen bromide-activated sepharose beads, as described earlier [65]. Purification was carried out at 4°C or in an ice bath. Cells were lysed with lysis buffer at pH 7.6 containing 20 mM Tris-HCl, 0.25% TritonX-100, 100 mM NaCl, 10 mM EDTA, and 1 tablet of protease and phosphatase inhibitors per 50 mL (cOmplete™ ULTRA Tablets Mini EDTA-free and PhosSTOP, Roche, Basel, Switzerland) and sonicated with a Vibracell (10 cycles, 30 s on and 1 min off, 50% active cycle). The lysate was centrifuged at $16,000\times g$ for 30 min, then the supernatant was filtered through a 0.22 μm membrane. The filtered lysate was then mixed with the beads grafted with MCP21 antibody and incubated overnight. The next day, the beads were washed with equilibration buffer (20 mM Tris HCl, 1 mM EDTA, 10% glycerol, 100 mM NaCl, pH 7.6) and eluted with equilibration buffer supplemented with 3 M NaCl. The eluate was concentrated down to 0.5 mL on centrifugal filters of 100 kDa MWCO and then separated using gel filtration chromatography. The chromatography was performed on a Superose 6 10/300 GL column, using TSDG buffer (10 mM Tris-HCl pH 7.0, 1 M KCl, 10 mM NaCl, 5.5 mM MgCl₂, 0.1 mM EDTA, 1 mM DTT, 10% glycerol). The fractions were assayed by proteasome enzymatic activity and the active proteasome fractions (eluted fraction between 10–14 mL) were pooled together. Buffer exchange with equilibration buffer and concentration of fractions were done on centrifugal filters of 100 kDa MWCO. Additional glycerol was added to reach 20% and smaller aliquots were made. Aliquots were snap-frozen in liquid nitrogen and stored at -80°C until use.

2.6. Purification of Proteasome from Caco2 Cells, BLCLs, Organoids and Crypts

MCP21 antibody (100 μg) was grafted and cross-linked (using 20 mM dimethyl pimelidate in 0.2 M triethanolamine, pH 8.2) onto Protein G MagBeads (Genscript) (100 μL of 25% slurry) using the manufacturer's protocol at room temperature. The purification was done at 4°C or in an ice bath. Samples were lysed with lysis buffer at pH 7.6 containing 20 mM Tris HCl, 0.25% TritonX-100, 10% glycerol, 100 mM NaCl, 10 mM EDTA, 10 mM ATP, 5 mM MgCl₂, and 1 tablet of protease and phosphatase inhibitors per 50 mL (cOmplete™

ULTRA Tablets Mini EDTA-free and PhosSTOP, Roche) and sonicated (Bioruptor Plus, Diagenode; 15 cycles, 45 s on and 15 s off) and then centrifuged at $16,000 \times g$ for 10–30 min. The supernatant (at least with 1–3 mg of total protein) was then mixed with the magbeads and incubated overnight. The next day, the beads were washed with equilibration buffer (20 mM Tris HCl, 1 mM EDTA, 10% glycerol, 100 mM NaCl, 2 mM ATP, 5 mM MgCl₂, pH 7.6) and eluted with equilibration buffer supplemented with 3 M NaCl. The eluate was concentrated on centrifugal filters of 100 kDa MWCO while the buffer was exchanged with 200 mM ammonium acetate pH 7.4. Samples were analyzed directly to LC-MS, if possible. Otherwise, small aliquots of 10 μ L were snap-frozen in liquid nitrogen and stored at -80 °C until use.

2.7. Detailed Top-Down LC-MS Analysis

The purified 20S aliquots were thawed and diluted (1:1) with 2% acetonitrile (ACN) and 0.02% formic acid (FA) in milliQ water. They were analyzed by online nanoLC using UltiMate 3000 RS autosampler and UltiMate 3000 RSLCnano LC system (ThermoScientific) coupled with an Orbitrap Fusion Tribrid mass spectrometer (Thermo Scientific) operating in positive mode through a Nanospray Flex™ Ion source ES072 (Thermo Scientific). Each sample (1–2 pmol) was loaded onto a reverse-phase C4-precursor column (300 μ m i.d. \times 5 mm; Thermo Fisher Scientific) at 20 μ L/min with loading buffer (milliQ H₂O with 2% ACN and 0.2% FA). After 3 min of desalting, the precolumn was switched online with an analytical C4 nanocolumn (in-house packed Reprosil-PUR C4 3 μ m, 75 μ m i.d. \times 15 cm) equilibrated in 95% solvent A (milliQ H₂O with 0.2% FA) and 5% solvent B (80% ACN with 0.2% FA and 20% milliQ H₂O). Proteins were eluted using a binary gradient ranging from 5% to 40% (5 min), then 40% to 99% (33 min), and finally back to 5% (13 min) of solvent B at a flow rate of 300 nL/min. The MS was operated in Intact protein application mode with the Xcalibur 4.5 software (Thermo Fisher Scientific). The spray voltage was set to 1900 V, the ion transfer tube temperature to 350 °C, the RF lens to 60%, the normalized AGC target at 75% and the maximum injection time at 50 ms. For the MS-only method, scans were acquired in the 700 to 2000 m/z range with the Orbitrap resolution set to 15,000 and using 10 μ scans for averaging. For the MS/MS method, the MS scans were acquired in the 1000 to 2000 m/z range with the resolution set to 7500 and using 10 μ scans for averaging. The data-dependent mode was based on the cycle time, with 3 s between the master scans. The quadrupole isolation window was set at 5 m/z and electron-transfer/higher-energy collision dissociation (ETDC) fragmentation was used at 25% collision energy. Activation was achieved with ETD with a reaction time of 5 ms, a reagent target of 7×10^5 , and a maximum reagent injection time of 200 ms. The normalized AGC target was set at 400% and the maximum injection time at 400 ms. The MSMS scans were acquired on normal mass range with the resolution set to 60,000 and with 3 μ scans.

The MS spectra were deconvoluted using RoWinPro software [55] and the results were visualized with VisioProtMS [66]. To determine the percentage of a particular proteoform, the sum of intensities from Rowinpro corresponding to each proteoform were attained and divided by the total sum of intensities corresponding to the subunit. In addition, MS/MS data were processed in Proteome Discoverer 2.3 (Thermo Scientific) to identify the proteoforms by sequence-matching the MS/MS fragments. A three-tier search was used for the processing workflow that contains an Absolute Mass Search with a narrow precursor mass tolerance of 100 Da, a BioMarker Search and another Absolute Mass Search with a large precursor mass tolerance of 1000 Da.

2.8. Label-Free Quantification in TD-MS using Relative Ionization Yields

The relative quantification was carried out using the intensity obtained after deconvolution of the raw data with UniChrom2 [67]. For each subunit, the intensities of known proteoforms were summed up. With the results coming from c20S or i20S purified from HEK-EBNA, the relative ionization yields (RIY) of each 20S subunit were calculated

by dividing their intensity with the average intensity of all the non-catalytic subunits (Equation (1)).

$$RIY_{Si} = \frac{A_{Si}}{\frac{1}{n} \sum A_{SnCS}} \quad (1)$$

where RIY_{Si} = relative ionization yield of a 20S subunit from pure c20S or i20S; A_{Si} = abundance of a 20S subunit from pure c20S or i20S; A_{SnCS} = abundance of non-catalytic 20S subunits (α 1-7, β 3,4,6,7) from pure c20S or i20S; and n = number of non-catalytic 20S subunits.

For the samples, the resulting 20S subunits' intensities were corrected by dividing by their respective RIY, then normalized with the average intensity of non-catalytic subunits (Equations (2) and (3)).

$$A_{Sx,corrected} = \frac{A_{Sx}}{RIY_{Si}} \quad (2)$$

$$C_{Sx} = \frac{A_{Sx,corrected}}{\frac{1}{n} \sum A_{SnCS,corrected}} \quad (3)$$

where $A_{Sx,corrected}$ = corrected abundance of subunit x in the sample; A_{Sx} = raw abundance of a subunit x in the sample; $A_{SnCS,corrected}$ = corrected abundance of non-catalytic 20S subunits (α 1-7, β 3,4,6,7) in the sample; and C_{Sx} = relative amount of 20S subunit in the sample.

These results were compared with the calculated amount from just applying normalization with the average intensity of all the non-catalytic subunits (i.e., without the correction with RIY). Two sets of RIYs were established from three to four technical replicates of measurements with three injections of c20S and i20S in Tris and ammonium acetate buffers (the two buffers that we usually use for proteasome) for comparison. The relative quantification was first applied on different mixes of pre-purified c20S and i20S (c20S/i20S: 10%/90%, 20%/80%, 30%/70%, 50%/50%, 70%/30%, 80%/20% and 90%/10%) and then on endogenous samples such as immunopurified 20S from IFN γ -treated Caco2 cells, intestinal crypts and PRAAS-related samples. The proportions of c20S and i20S (which include all the immuno-containing 20S here) correspond to the relative abundance of β 5 and β 5i, respectively. Outliers were determined using the interquartile range method. Accuracy was calculated by finding the difference between the experimental and theoretical value divided by the theoretical value, while the coefficient of variation was the ratio of standard deviation to the mean in percentage.

2.9. Detailed Bottom-Up LC-MS Analysis

Lysates or eluents were supplemented with SDS to reach a final concentration of 5%, sonicated (15 cycles, 45 s ON and 15 s OFF at 10 °C) and centrifuged at 16,000 \times g for 10–30 min. Supernatant was then reduced with 100 mM tris(2-carboxyethyl)phosphine and alkylated with 400 mM 2-chloroacetamide at 95 °C for 5 min. Each sample was loaded on an S-trap spin column (Protifi, Fairport NY, USA), according to the manufacturer's instructions, and digested with trypsin (Promega, Madison, WI, USA), corresponding to 2% of total protein weight (with a minimum of 1 μ g), overnight at 37 °C. Digested peptide extracts were analyzed by online nanoLC using an UltiMate 3000 RSLCnano LC system (Thermo Scientific) coupled with an Orbitrap Fusion Tribrid mass spectrometer (Thermo Scientific) operating in positive mode. Each sample (1.0–2.5 μ g peptides as analyzed by Pierce quantitative fluorometric peptide assay) was loaded onto a 300 mm ID 5 mm PepMap C18 pre-column (Thermo Scientific) at 20 ml/min in 2% ACN, 0.05% trifluoroacetic acid. After 5 min of desalting, peptides were on-line separated on a 75 mm ID 50 cm C18 column (in-house packed with Reprosil C18-AQ Pur 3 mm resin, Dr. Maisch; Proxeon Biosystems, Odense, Denmark) equilibrated in 95% buffer A (0.2% FA), with a gradient increased to 25% buffer B (80% ACN, 0.2% FA) for 75 min, then to 50% B for 30 min and then to 98% B for 10 min; they were held for 15 min before returning to starting conditions for 25 min, totaling an entire run time of 160 min at a flow rate of 300 nL/min. The instrument was operated in data-dependent acquisition mode using a top-speed approach (cycle time of 3 s). Survey scans MS were acquired in the Orbitrap over 400–1500 m/z with a resolution of 120,000,

and a maximum injection time (IT) of 50 ms. The most intense ions (2+ to 7+) were selected at 1.6 m/z with quadrupole and fragmented by higher energy collisional dissociation (HCD). The monoisotopic precursor selection was turned on, the intensity threshold for fragmentation was set to 50,000, and the normalized collision energy (NCE) was set to 35%. The resulting fragments were analyzed in the Orbitrap with a resolution of 30,000. Dynamic exclusion was used within 60 s with a 10 ppm tolerance. The ion at 445.12003 m/z was used as the lock mass. The Mascot (Mascot server v2.8.1, Matrix Science, Boston, MA, USA; <http://www.matrixscience.com> (accessed on 3 June 2021)) database search engine was used for peptide and protein identification. Mass tolerance for MS and MS/MS was set at 10 ppm and 20 mmu, respectively. The enzyme selectivity was set to full trypsin with two missed cleavages allowed. The protein modifications were fixed carbamidomethylation of cysteines, variable oxidation of methionines, variable phosphorylation of serine, threonine and tyrosine, and variable acetylation of protein N-terminus. The UniProt proteome for both human and mouse was used as the database. The result files were then imported into Proline [68] for validation with false discovery rate (FDR) of $\leq 1.0\%$ and label-free quantitation. Iterative alignment computation was applied using peptide identity with three as the maximum number of iterations. Alignment smoothing was carried out with a landmark range with 50 landmarks and 50% sliding window overlap. For the master map creation, the mapping tolerances were 5 ppm and 60 s for the m/z and time, respectively. For the statistics parameters, the *t*-test *p*-value of 0.01 was applied on both peptide and protein profile significant analysis. Only specific peptides were used, and the median ratio fitting was chosen as the abundance summarizer method. Normalization, missing values inference, *t*-test and *z*-test were also applied. IBAQ values were calculated by dividing the abundances with the number of observable peptides. The stoichiometry and relative amount of each 20S subunit, activators and interacting proteins were calculated using IBAQ values, as previously described by Fabre et al. [51]. For the treated Caco2 cells, mean and standard deviations were calculated from three biological replicates, while for the BLCLs, they were calculated from three injection replicates. Statistical difference was determined based on a one-way ANOVA with Tukey's HSD test.

2.10. Proteasome Activity Assay

The activity assay was performed in 96-well black plates (Greiner Bio-One, Kremsmünster, Austria). A total of 10 μ L of clear lysate (corresponding to 10 μ g total proteins) was diluted with 40 μ L of 100 mM Tris-HCl pH 8 buffer. Then, 50 μ L of 100 μ M fluorogenic peptide substrate, Suc-LLVY-AMC, Boc-LRR-AMC or z-LLE-AMC, to probe for chymotrypsin-, trypsin- or caspase-like activities, respectively, were added. The fluorescence intensities at $\lambda_{Ex}/\lambda_{Em}$ of 360/460 nm and at 37 °C were measured in a microplate fluorimeter (CLARIOstar, BMG Labtech, Ortenberg, Germany) for 12 cycles, with one reading every 5 min. The slope of the increase in fluorescence intensity over time (within linear range) was calculated, and normalization was done using the average slope for the controls. Mean and standard deviation were calculated from the three technical replicates. Statistical difference was determined based on a one-way ANOVA with Tukey's HSD test.

3. Results

3.1. Establishing 20S Proteoform from Different Biological Materials

3.1.1. Tri-Phosphorylated $\alpha 7$ (PSMA3) in Human 20S Identified by TD-MS

PTMs such as phosphorylation have been linked to either up- or down-regulation of proteasome activity [21,22]. In humans, phosphosites have been reported in 20S subunits including $\alpha 2$, $\alpha 4$, $\alpha 7$, $\beta 1$ and $\beta 7$, but the $\alpha 7$ phosphorylated form, which was found to regulate 26S stability [69] and Ecm29 binding [49], is by far the one that is detected in the widest variety of biological samples [8,22,55,70–72]. In order to gain better insight into human 20S proteoforms, we analyzed immunopurified 20S from HEK-EBNA cells expressing either c20S or i20S by TD-MS [2]. Importantly, as the immunopurification strategy used here targets $\alpha 2$, a subunit shared by all 20S proteasome subtypes, the 20S

core particles analyzed in this work may correspond to in cellulose free, regulator-associated 20S proteasomes, or assembling 20S proteasomes [51]. In line with our previous work, we only observed phosphorylation of $\alpha 7$ [8,55]. For c20S, the acetylated [2-255] (28,344 Da) and mono-phosphorylated [2-255] (28,424 Da) forms that have been previously reported were both observed in MS (Figure 1A) and sequenced by MSMS (Figure 1B,C). Interestingly as shown in Figure 1A, additional proteoforms at 28,529 Da and 28,600 Da, were also observed. The proteoform at 28,529 Da exhibited a + 96 Da mass difference compared to the full-length $\alpha 7$ [1-255], reflecting to a phosphorylation (+80 Da) and oxidation (+16 Da). On the other hand, the proteoform at 28,600 Da (one of the major proteoforms observed here) showed a + 298 Da mass excess compared with the 28,344 Da proteoform (acetylated $\alpha 7$ [2-255]), possibly corresponding to three phosphorylations and one oxidation (25 ppm mass error based on the MW of the precursor in MSMS analysis as shown in Figure 1D). The matched b- and c- ion fragments confirmed that it corresponded to $\alpha 7$; however, the lack of y- and z-ion fragments limited the localization of the additional phosphorylations and oxidation (Figure 1D). Note that the placement of the phosphorylation sites at S243 and S250 is based on BU proteomics literature [71–74], while phosphorylation at S142 is based on prediction by NetPhos3.1 (score 0.977) [75,76] (Figure S1A) and the oxidation of the C-terminal methionine was previously reported by our group [77]. This suspected tri-phosphorylated form was not specific to the c20S since it was also observed in i20S as the main proteoform when it is freshly purified (Figure S1B,C). However, it was found to be unstable upon storage, from 91% of total $\alpha 7$ after purification, down to 9% after three months at -80°C (Figure 1E,F), which can be related to the previously observed truncations of $\alpha 4$ and $\alpha 4\text{s}$ upon storage [9]. Furthermore, this putative tri-phosphorylated state was highly unstable under acidic conditions (0.2% formic acid, 2% acetonitrile), as its abundance decreased during the course of three consecutive injections (i.e., 92%, 44% and 10%), while the amount of the mono-phosphorylated proteoform increased (i.e., 1%, 32% and 69%), becoming the main $\alpha 7$ proteoform (Figure S2). These results indicate that human $\alpha 7$ is constitutively tri-phosphorylated but includes two highly labile phosphorylations, other than the previously described S250 phosphosite.

3.1.2. Mutations in 20S Subunits in PRAAS Patients and Their Effect on 20S Assembly

PRAAS mutations have been identified in genes encoding 20S non-catalytic subunits such as $\alpha 7$ and $\beta 7$, and immuno-catalytic subunits $\beta 5\text{i}$, $\beta 1\text{i}$ and $\beta 2\text{i}$ [18,27–32,35]. Previous work used immunoblotting for tagged proteins and native-PAGE analysis to assess the impact of the mutation on 20S composition and assembly, a strategy that requires the long process of cell transfection and expansion as well as the challenging development of specific antibodies [18,35]. To quickly establish proteoform footprinting in endogenous samples and determine whether these mutations affect 20S assembly, we analyzed immunopurified 20S from BLCLs expanded from PRAAS patients and healthy controls with TD-MSMS, which is fast and has a greater specificity compared to antibody-based methods. We analyzed nine samples: three PRAAS patients, Patient A ($\beta 5\text{i}$ p.(T75M) homozygous), Patient B (digenic: $\beta 5\text{i}$ p.(T75M) and $\alpha 7$ p(R233del)), and Patient C (compound heterozygous $\beta 7$ p.(D212_V214del) and $\beta 7$ 5'UTR c.-9G>A); the father and mother of Patient C who are both clinically healthy but have $\beta 7$ D212_V214del and $\beta 7$ 5'UTR c.-9G>A mutations, respectively, and four other healthy controls.

Patient A had two proteoforms in the $\beta 5\text{i}$ subunit that, as expected, harbored the p.(T75M) mutation, one at 22,689 Da, that had a relative abundance of 90% and corresponds to the mature form [73-276], and one at 22,705 Da with a relative abundance of 10%, which is its mature oxidized counterpart (Figure 2A). These two proteoforms were confirmed by their MWs (<1 Da mass accuracy) and MSMS sequencing (Figure 2B,C). These results confirm that (1) the mutation is homozygous, as no WT subunit with an expected MW of 22,659 Da was observed, and (2) the mutation does not impede the incorporation of the $\beta 5\text{i}$ subunit into the 20S in the course of assembly. However, despite proper incorporation, a significant decrease in chymotrypsin-like (p -value < 0.0001) but not trypsin-like and

caspace-like activity was observed (Figures 2D and S3A,B), as was previously reported [27]. Additionally, we observed that the MW of $\beta 1i$ was 20 Da lower than that expected for the WT isoform (21,276 Da). By adding in our database all the 20S subunit variants present in UniProt, we identified the p.(R60H) SNP as the best fit for our MSMS data (Figure 2E). This highly prevalent allele is very common (allele frequency of 0.24, with 8575 homozygotes in the gnomAD database) and has no association with diseases, but would have probably been missed by a classical BU approach.

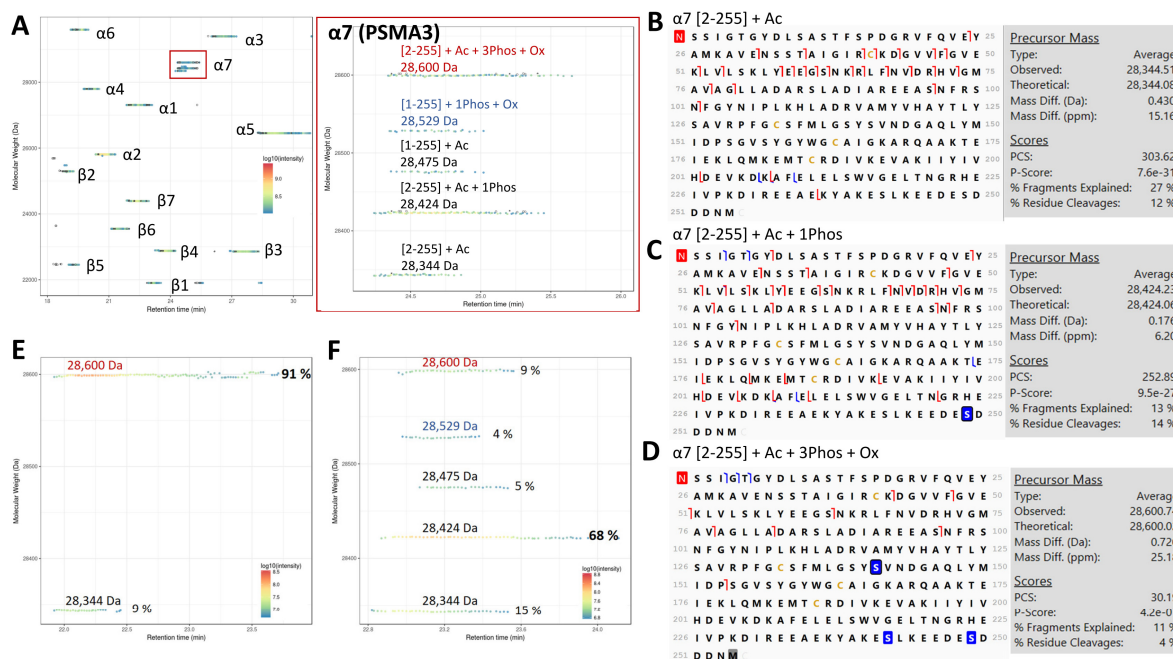


Figure 1. TD-MS identification of proteoforms in human constitutive 20S (c20S) proteasome purified from HEK-EBNA cells: (A) Proteoform map visualized in VisioProtMS, showing the c20S subunits zoomed to the different proteoforms of $\alpha 7$ (PSMA3) as shown by the overlapped LC-MS and MS/MS traces. Figures in brackets indicate the first and last amino acids in the sequence of the corresponding detected proteoform. Ac = acetylation, Ox = oxidation, Phos = phosphorylation; (B–D) MSMS top-down sequencing using Proteome Discoverer of the three main proteoforms of $\alpha 7$ [2-255]: acetylated at 28,344 Da, mono-phosphorylated at 28,424 Da and tri-phosphorylated at 28,600 Da. Acetylation, oxidation and phosphorylation sites are highlighted in red, gray, and blue, respectively. Red and blue lines correspond to c-/z- and b-/y- ions, respectively. (E,F) Changes in the abundances of $\alpha 7$ proteoforms just after purification and after three months of storage at -80°C , respectively. % correspond to the abundance of the proteoform relative to the sum of intensities corresponding to the subunit.

Complementary BU-MS analysis indicates a slight decrease (5 %) in the abundance of 20S in the lysate of this patient-derived BLCL compared to those from healthy donors (Figure S4A). Label-free BU-MS analysis after 20S immunopurification reports a 1.5-fold increase in the amount of assembling 20S (based on the abundance of 20S-associated assembling chaperones, Figure S4B,C) and no major difference in terms of co-immunopurified major 20S-associated proteins, apart from a threefold higher interaction with PA28 $\alpha\beta$ compared to healthy donors (Figure S4D). Altogether, these results indicate that mutation of the catalytic p.(Thr75) mainly affects $\beta 5i$ activity with little impact on its incorporation, structure and subsequent 20S interactome.

Patient B harbors digenic mutations in $\beta 5i$ (p.(T75M)) and $\alpha 7$ (p.(R233del)), respectively, and the corresponding proteoform maps are shown in Figure 3A,B. In this case, both the mature WT (22,659 Da, 51% relative abundance) and mature p.(T75M) mutant $\beta 5i$ (22,689 Da, 41% relative abundance) were observed by TD-MS. Some partial oxidation was also observed for both the WT (22,675 Da, 6% relative abundance) and p.(T75M)

mutant (22,705 Da, with 2% relative abundance). Both the WT and p.(T75M) proteoforms were confirmed by their MWs (<1 Da mass difference) and by TD-MSMS sequencing (Figures 3C,D and S5). The relative abundance of the mutated ($43 \pm 3\%$) was slightly lower than for the WT ($57 \pm 3\%$), but clearly confirms that Patient B is heterozygous for the p.(T75M) mutation. Four $\alpha 7$ proteoforms were also observed, including the three main WT forms (acetylated at 28,344 Da, mono-phosphorylated at 28,424 Da, and tri-phosphorylated at 28,600 Da) and a lower abundant proteoform at 28,186 Da, which may correspond to the oxidized [2-255] form, with the expected deletion of p.(R233). Due to the low abundance of this p.(R233del) proteoform (4% of the total $\alpha 7$), it was not selected for MSMS sequencing. The only detected proteoform was the most abundant (79%) WT acetylated proteoform (Figure 3E). These results indicate that (1) Patient B is heterozygous for the T75M $\beta 5i$ mutation, since the WT proteoform was also observed in similar abundance to the T75M proteoform, (2) there is indeed an incorporation of the T75M $\beta 5i$ subunit in 20S complexes, albeit to a lower extent when compared to WT $\beta 5i$, as previously suggested [18], and (3) the deletion of p.(R233) in $\alpha 7$ resulted in almost (4%) no incorporation of this proteoform in the 20S, as shown by Brehm et al. [18], thus resulting in reduced incorporation in the 20S (since $96 \pm 1\%$ of the signal corresponds to the WT form). A significant decrease in chymotrypsin- and trypsin-like activities was observed in the lysate from Patient B (Figures 3F and S3A); this is similar to what had already been reported [18]. The caspase-like activity was also decreased, albeit not significantly (Figure S3B). The $\beta 1i$ p.(R60H) SNP was also found in Patient B, as confirmed by TD MSMS sequencing (Figure 3G).

Similarly to Patient A, our complementary BU-MS analysis indicated only a slight change (3 % decrease) in 20S abundance in the lysate of Patient B (Figure S4A), whereas previous work reported a decrease in proteasome content due to reduced expression of the mutated $\alpha 7$ subunit [18]. BU-MS label-free analysis after 20S immunopurification also suggested a similar amount of assembling 20S (Figure S4B,C) and no major change in interactions with the major 20S-associated proteins (Figure S4D). Altogether, these results confirm that the mutation of the catalytic p.Thr75 affects mainly $\beta 5i$ activity, with little impact on its incorporation, structure and subsequent 20S interactome. Interestingly, the reduction in chymotrypsin-like activity for this heterozygous Patient B (Figure 3F), was ~half of that observed for the homozygous Patient A (Figure 2D). Furthermore, our results show that the R233del mutant of $\alpha 7$ is not incorporated in 20S proteasome (only by 4%). In order to discriminate between quantity and assembly defects, we next attempted to quantify the p.(R233del) vs. WT $\alpha 7$ in the lysate of Patient B, by semi-quantifying proteo-specific peptides. However, p.R233 is surrounded by two other trypsin cleavage sites (K/DIR/EEAEK/), meaning that the resulting peptide (DIR) is very small. Deletion of p.R233 removes a trypsin cleavage site and would generate the peptide DIEEAEK that could potentially be observed and quantified by our approach, but this is not the case for the very small DIR peptide present in the WT. However, the fact that no changes were detected in the levels of assembling 20S (Figure S4C), suggests that there was no incorporation deficiency, but rather either a reduced protein expression or a decreased stability of this mutated $\alpha 7$.

For Patient C, harboring compound heterozygous mutations p.(D212_V214del) and 5'UTR c.-9G>A in subunit $\beta 7$, the TD-MS proteoform map showed MWs corresponding to mature WT $\beta 7$ [46-264] at 24,392 Da (main proteoform with 75% relative abundance) and its oxidized form at 24,408 Da (Figure 4A). These two proteoforms were confirmed by TD-MSMS sequencing with only <1 Da MW difference on the precursors (Figure 4B,C). When overlapping the $\beta 7$ proteoform maps of Patient C with his parents (Figure 4D), we observed very similar results between Patient C and his mother, who carries the 5'UTR c.-9G>A SNP. In the case of the father with the p.(D212_V214del) mutation, $\beta 7$ was observed at 24,380 Da and 24,396 Da, which are both 12 Da lower than the corresponding MWs in Patient C and his father. According to the variants present in the UniProt database, this 12 Da difference may correspond to the replacement of Ile234 by a Thr residue, which was further confirmed by TD-MSMS sequencing, in the father only (Figures 4E and S6). This SNP has an allele frequency of 0.19, with 6086 homozygotes in the gnomAD database.

Interestingly, with the complementary BU-MS results, both Patient C and his father had five to 15 times higher levels of the 20S-associated chaperones (PAC1-PAC2, and POMP), than the controls (Figure S4C), which confirms previous data [18] and indicates that the p.(D212_V214del) mutation impedes $\beta 7$ maturation, inducing a stalling of the assembly process. This is in accordance with the observed lower amounts of 20S proteasome (about a 15% decrease compared to controls) in the corresponding lysates (Figure S4A) that is likely caused by the destabilization of the C-terminal tail of $\beta 7$, which functions as a clamp between the two halves of the 20S proteasome complex [18,78]. Finally, unlike Patients A and B, Patient C shows only WT $\beta 1i$. However, TD-MS analysis of his mother shows both WT and p.(R60H) proteoforms, which was also the case in two healthy patients (Figure S7B). The results of Patient C and his parents thus show that (1) there is indeed no incorporation of the p.(D212_V214del)-mutated $\beta 7$ subunit into the 20S complexes, as we only observed the WT forms; (2) the p.(D212_V214del) mutation on $\beta 7$ results in a partial stalling of the 20S proteasome assembly process; and (3) the father of Patient C in addition to the p.(D212_V214del) also carries the p.(I234T) SNP on $\beta 7$, which does not impede 20S incorporation and was not seen in Patient C.

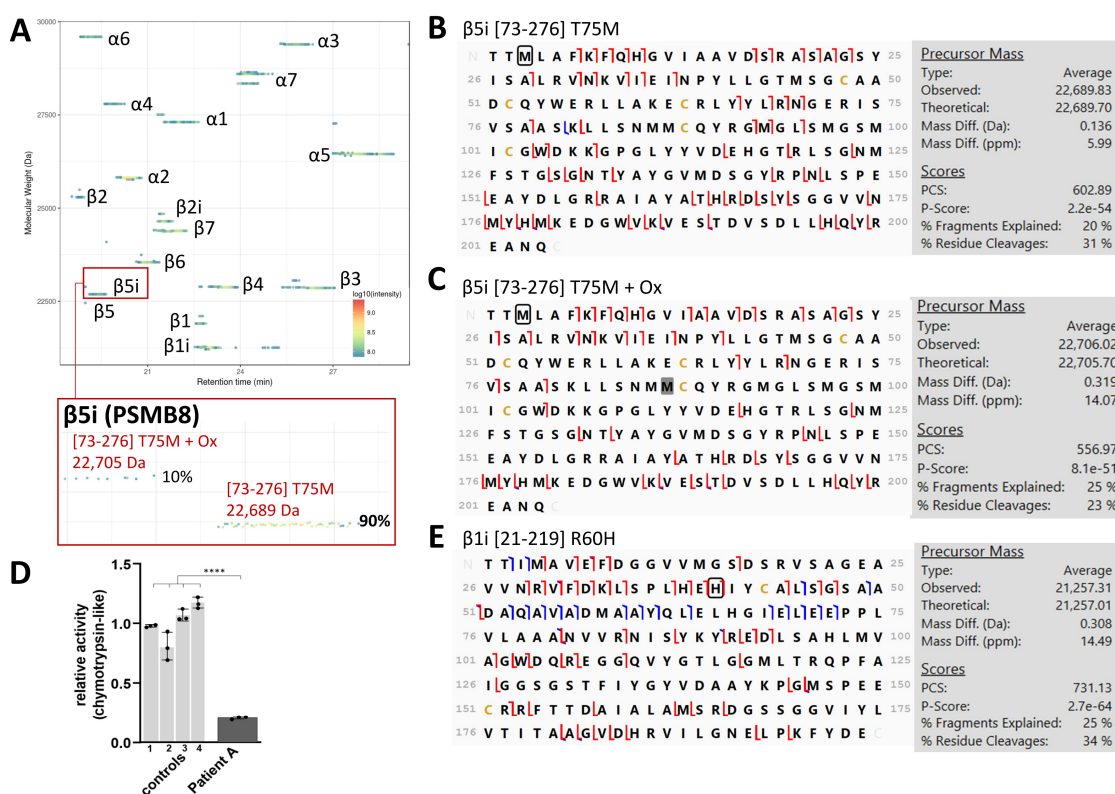


Figure 2. Characterization of the 20S mature proteoforms from PRAAS Patient A with $\beta 5i$ T75M homozygous mutation and $\beta 1i$ R60H SNP by TD-MS: (A) Proteoform map using VisioProtMS showing $\beta 5i$ [73-276] T75M at 22,689 Da and 22,705 Da (oxidized form). Figures in brackets indicate the first and last amino acids of the mature $\beta 5i$ sequence. Ox = oxidation. % correspond to the abundance of the proteoform relative to the sum of intensity values corresponding to the subunit; (B,C) MSMS top-down sequencing of the mature [73-276] and mature oxidized forms of $\beta 5i$, respectively. Note that the oxidation, highlighted in gray, was manually localized on one of the methionines in the S153W177 stretch, based on the highest number of c- and z- fragments. The T75M mutation (circled in black) is clearly confirmed by many c- fragments. Red and blue lines correspond to c-/z- and b-/y- ions, respectively; (D) Relative chymotrypsin-like activity of the patient compared to healthy controls using Suc-LLVY-AMC substrate analyzed in triplicates (**** p -value < 0.0001 from a one-way ANOVA with Tukey’s HSD test); and (E) MSMS top-down sequencing of the main R60H mature [21-219] $\beta 1i$ proteoform. H60 is circled in black.

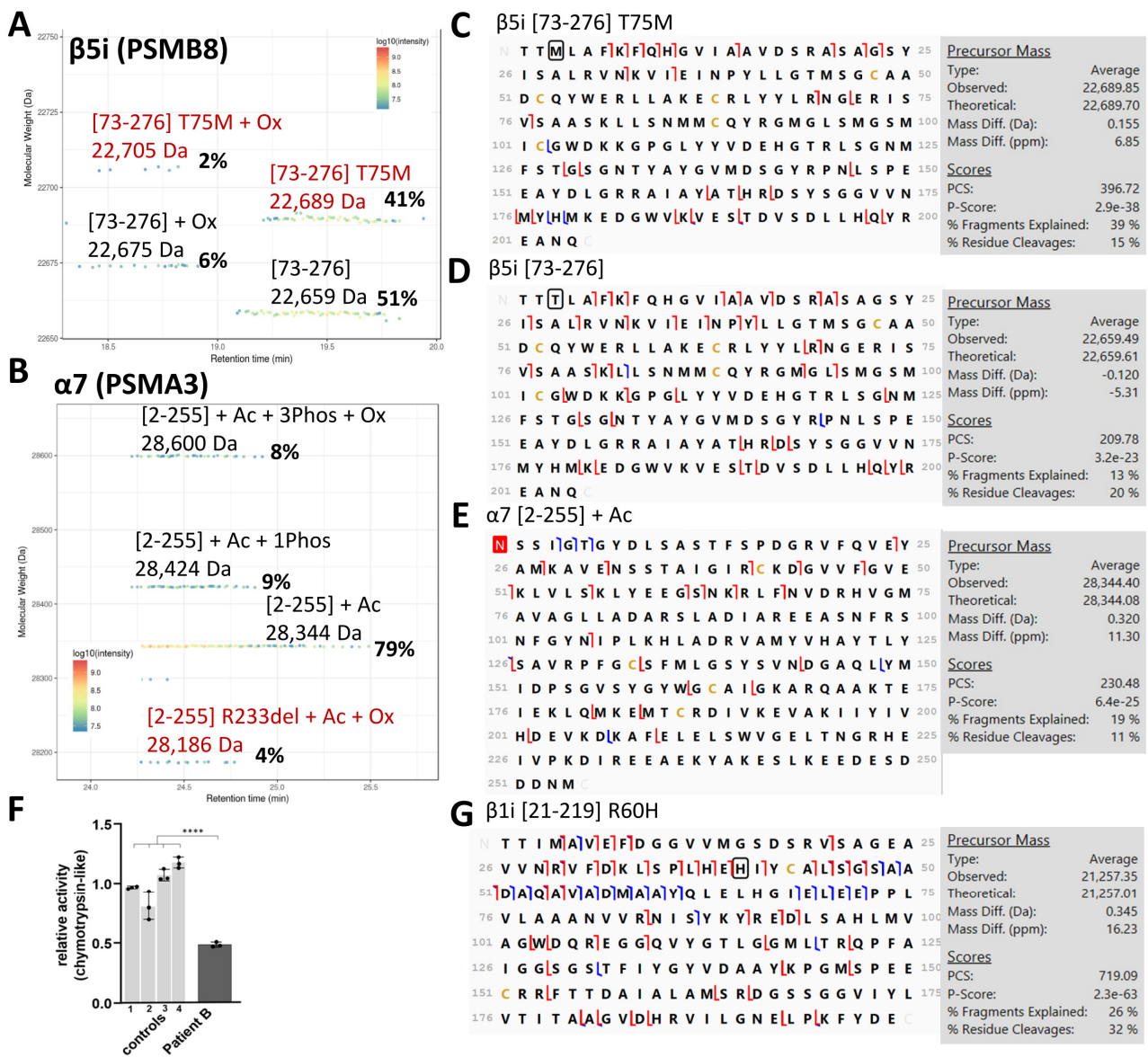


Figure 3. Characterization of the mature 20S proteoforms from PRAAS Patient B with $\beta 5i$ (*PSMB8*) T75M and $\alpha 7$ (*PSMA3*) R233del mutations by TD-MS: (A,B) Proteoform map using VisioProtMS showing (A) both the $\beta 5i$ [73-276] wild-type (WT) and T75M at 22,659 Da and 22,689 Da, respectively, and (B) $\alpha 7$ [2-255] WT (acetylated, monophosphorylated and triphosphorylated forms) and R233del (with acetylation and oxidation) at 28,186 Da. Figures in brackets indicate the first and last amino acids in the sequence of the corresponding detected protein. Ac = acetylation, Ox = oxidation, Phos = phosphorylation. % correspond to the abundance of the proteoform relative to the sum of intensity values corresponding to the subunit; (C–E) MSMS top-down sequencing using Proteome Discoverer of the (C) T75M and (D) WT mature [73-276] forms of $\beta 5i$, and the (E) acetylated form of $\alpha 7$ (without Met1, acetylation is highlighted in red). Red and blue lines correspond to c-/z- and b-/y-ions, respectively. (F) Relative chymotrypsin-like activity of the patient compared to healthy controls using Suc-LLVY-AMC substrate analyzed in triplicates (**** p -value < 0.0001 from a one-way ANOVA with Tukey’s HSD test); and (G) MSMS top-down sequencing of the main R60H mature [21-219] $\beta 1i$ proteoform. H60 is circled in black.

3.1.3. Detection of Immuno Catalytic Subunits in Different Complex Samples by TD-MS

The immuno subunits of the proteasome are abundantly expressed in immune cells and they can also be induced upon exposure to oxidative stress and proinflammatory stimuli. To monitor their expression and to test the sensitivity of our TD-MS workflow, we

applied our pipeline to immunopurified 20S from samples of increasing complexity such as IFN γ -treated and non-treated Caco2 cells, healthy airway organoids, and intestinal crypts.

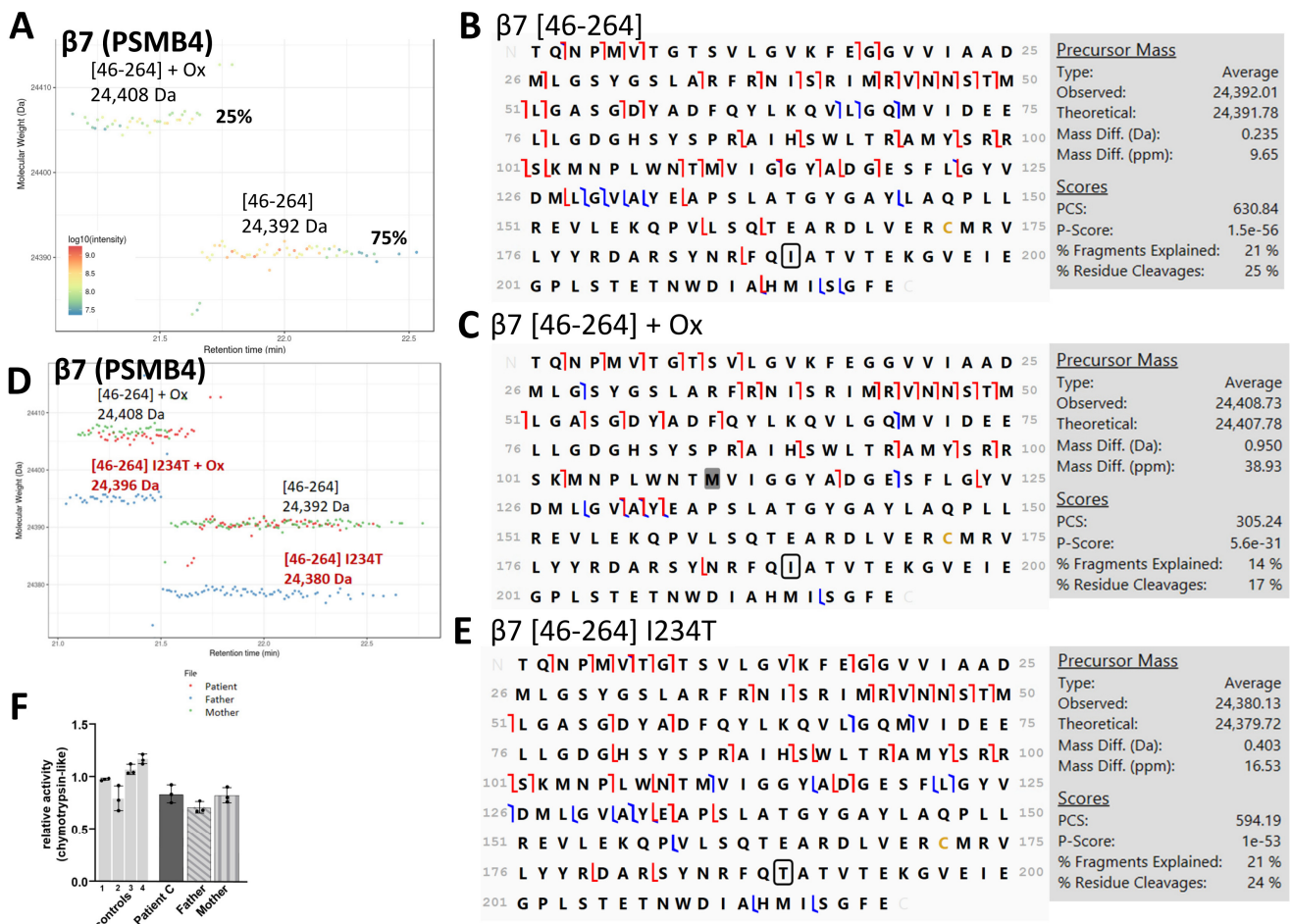


Figure 4. Identification of the mature $\beta 7$ (PSMB4) proteoforms of 20S from PRAAS Patient C with $\beta 7$ D212_V214del and $\beta 7$ 5'UTR c.-9G>A mutation by TD-MS: (A) Proteoform footprint using VisioProtMS showing only the wild-type $\beta 7$ [46-264] mature at 24,392 Da and its oxidized form at 24,408 Da. Ox = oxidation. % corresponds to the abundance of the proteoform relative to the sum of intensity values corresponding to the subunit; (B,C) MSMS top-down sequencing using Proteome Discoverer of the (B) mature [46-264] and (C) mature plus oxidation proteoforms (note that the oxidation, highlighted in gray, was manually localized on one of the methionines in the middle of the sequence, based on the highest number of c-/z- and b-/y- fragments). Only the mature amino acid sequence of $\beta 7$ is displayed. Red and blue lines correspond to c-/z- and b-/y- ions, respectively; (D) Overlapped proteoform maps of the patient and the parents revealing the -12 Da difference in the major $\beta 7$ proteoform of the father (24,380 Da vs. 24,392 Da), which may correspond to I234T SNP (circled in black); (E) MSMS top-down sequencing of the main proteoform of the father with possible I234T SNP; and (F) Relative chymotrypsin-like activity of the patient and the parents compared to healthy controls using Suc-LLVY-AMC substrate analyzed in triplicates.

Before using TD proteomics, to see the effect of inflammation on the 20S proteoforms, we monitored the expression of the six catalytic subunits in the lysate by label-free BU quantification after treatment with interferon- γ (IFN γ), tumor necrosis factor- α (TNF- α), lipopolysaccharide (LPS), interleukin-6 (IL-6) and interleukin-1 β (IL-1 β). Comparison of the median of all the peptide intensities divided by the number of observable peptides (iBAQ [79]) of each subunit revealed that the c20S catalytic subunits were replaced by their i20S counterparts using 10 ng/mL of IFN γ for three days (Figure 5A). The other

cytokine treatments failed to upregulate the i20S, as evidenced by PCR using IFN γ , TNF α and LPS [80].

We then treated Caco2 cells with 10 ng/ml IFN γ for 7 days to compare the proteasome TD-MS footprints before and after induction of the i20S. As expected, c20S was expressed constitutively in Caco2 cells and we observed a decrease in the signal of the standard catalytic subunits that were replaced by the i20S subunits upon treatment with IFN γ (Figure 5B).

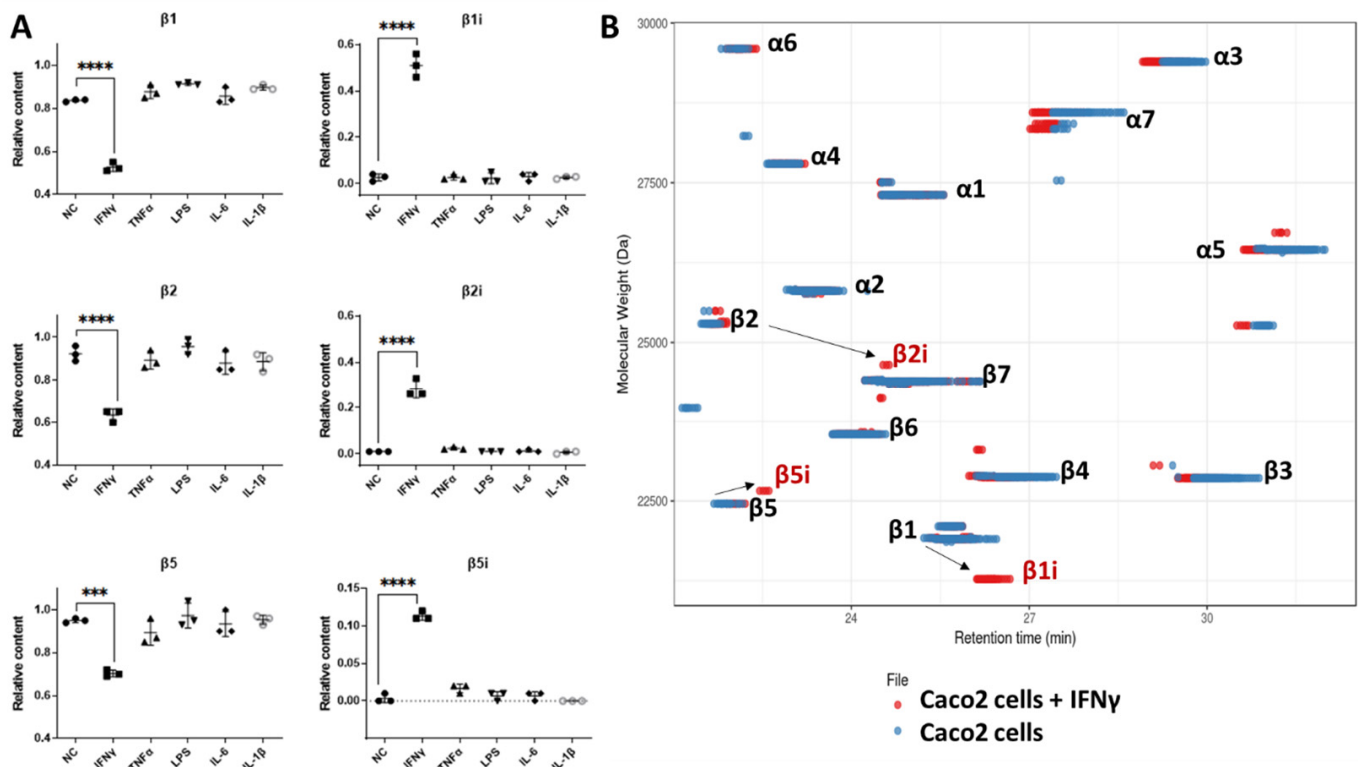


Figure 5. Induction of 20S immuno subunits in Caco2 cells with cytokines: (A) Relative amount of c20S and i20S catalytic subunits in the lysate by bottom-up proteomics (intensity-based absolute quantification or iBAQ) upon incubation with different cytokines (10 ng/ml IFN γ , 100 ng/mL TNF- α , 100 ng/mL IL-6, 100 ng/mL IL-1 β , 10 μ g/mL LPS). (B) Overlapped proteoform maps of immunopurified 20S from Caco2 cells with (in red) and without (in blue) IFN γ treatment (10 ng/mL for 7 days of treatment) analyzed with TD-MS showing the induction of immuno subunits. (***p*-value < 0.001 and *****p*-value < 0.0001 from a one-way ANOVA with Tukey's HSD test).

In healthy airway organoids, $\beta 1i/\beta 2i/\beta 5i$ subunits were detected even without IFN γ induction (Figure 6A). These airway organoids are composed mainly of epithelial cells such as ciliated, club, basal and goblet cells, and i20S has already been identified in nonimmune lung cells under normal conditions [81,82]. Although the function of the i20S in these cells is not fully explained, its implication in bronchial epithelial cell differentiation has already been reported [83].

Next, we attempted to immunopurify 20S proteasomes from crypts derived from partial resection of the intestinal tract from two patients. In a first attempt, starting from ~15,000 crypts (~1 mg protein) from a healthy donor allowed us to characterize only 12 out of 17 proteasome subunits (Figure 6B), thus demonstrating the limits of detection with this method. We repeated the experiment, starting from ~50,000 crypts (~3 mg) from a patient with suspicion of colorectal cancer, which enabled us to generate a full proteoform map containing both the c20S and i20S catalytic subunits (Figure 6C). Note that $\beta 5$ was not shown, as its intensity was below the threshold set for visualization. Visual comparison of the intensities of the subunits showed that this sample mostly contained the i20S. Overall,

these results indicate that our TD-MS workflow is sufficiently sensitive to monitor the incorporation of the i20S, not only in biological models such as cells and organoids, but also in biopsy samples.

3.2. Relative TD Label-Free Quantification of c20S and i20S in Complex Mixtures

As mentioned previously, current quantitative TD-MS approaches do not take into account ionization yields, because they either compare two different proteoforms of the same gene and assume that they have similar ionization yield, or perform differential analysis by comparing the signal intensity of each proteoform in various samples (after signal normalization). Here, we set out to quantify the relative abundance of each 20S subunit within a single acquisition. To this end, we first established the relative ionization yield (RIY) of each c20S and i20S subunit by spraying pure c20S and i20S and different mixes of known composition (see Section 2 and Supplementary Materials Figures S8–S12).

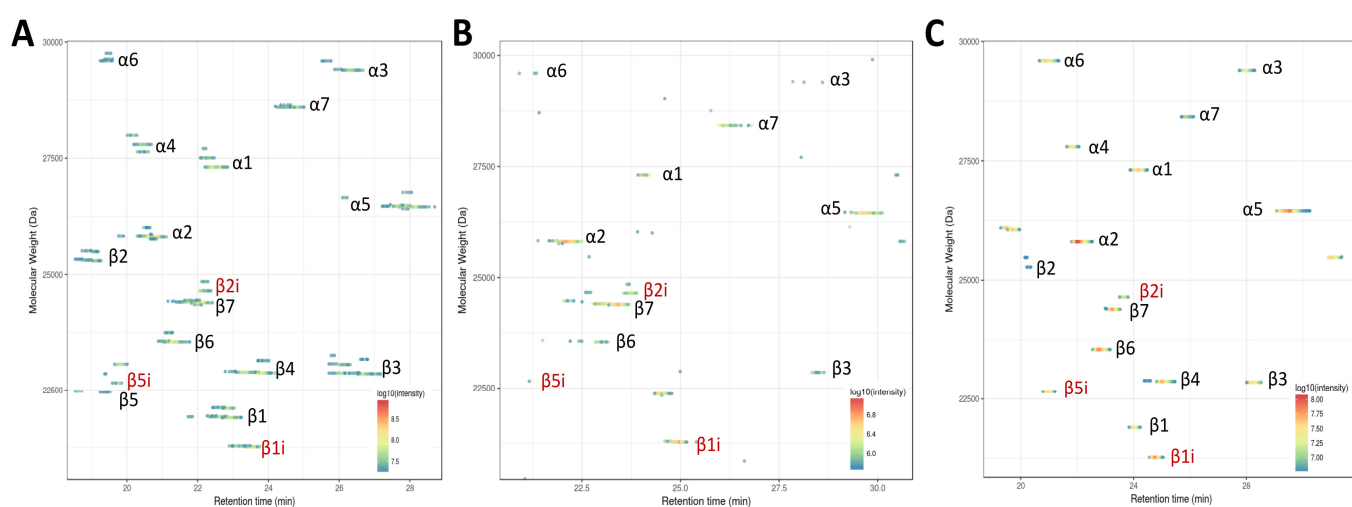


Figure 6. Proteoform map using VisioproMS showing the TD-MS identification of the immune subunits on immunopurified 20S from different biological samples such as: (A) airway organoids derived from normal lung tissue; and (B,C) biopsies containing 15,000 and 50,000 intestinal crypts, respectively.

In order to further benchmark our approach, we compared the label-free quantification obtained by BU-MS and by TD-MS with and without application of the previously established RIY (Figure S13). In all tested cases (Caco2 cells, intestinal crypts and PRAAS patients), the application of the RIY allowed us to obtain results that were in better agreement with the label-free BU-MS quantification, but without the need to perform trypsin digestion, and with the additional information from the proteoform footprint (see Supplementary Materials Figure S13).

We thus detected the following using this label-free TD-MS quantification with RIY correction: $85\% \pm 7\%$ i20S in Caco2 cells after 11 days of IFN γ treatment, $90\% \pm 9\%$ i20S in the intestinal crypt sample from normal tissue of a patient with suspicion of cancer, and an average of $80\% \pm 11\%$ i20S in all the BLCL derived from healthy and diseased patients (Figures 7 and S13).

These results indicate that (1) relative quantification of $\beta 5/\beta 5i$ signal intensities in TD-MS can be used to estimate the c20S and immuno-containing 20S levels in endogenous samples; and (2) the application of RIY correction on raw abundances is required to determine a better estimate than one achieved by just performing the usual normalization.

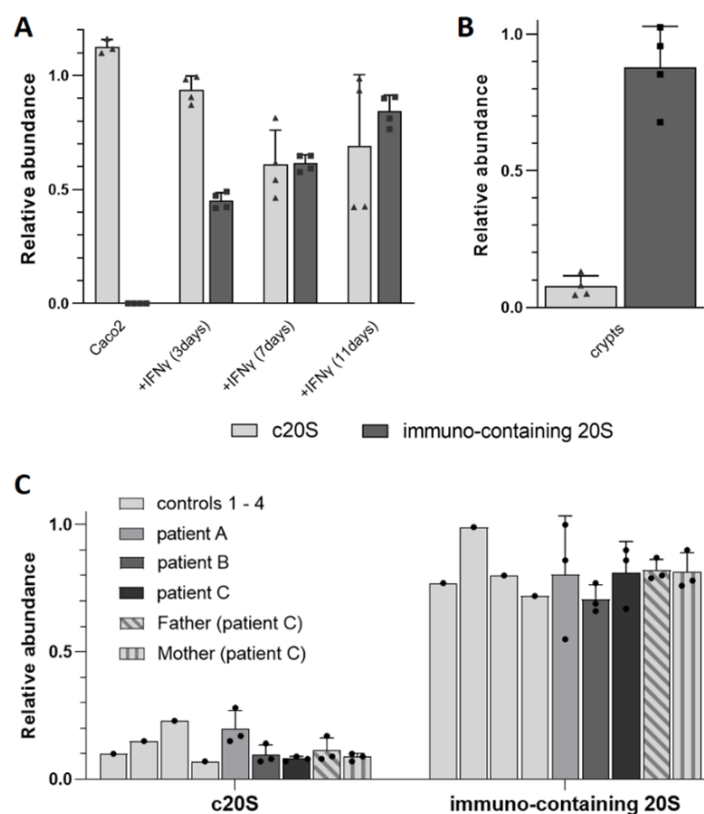


Figure 7. Relative TD label-free quantification of c20S and immuno-containing 20S subunit immunopurified from different samples: (A) Caco2 cells (\pm IFN γ), (B) intestinal crypts and (C) BLCLs derived from PRAAS patients and healthy controls.

4. Discussion

Our studies reported in this manuscript showed the advantages and current limitations of 20S immunopurification followed by TD-MS to unravel and semi-quantify its different proteoforms including PTMs, proteasome subunit mutations/SNPs and incorporation of i20S catalytic subunits.

In 20S proteasome immunopurified from HEK cells, Caco2 cells, BLCL from PRAAS patients and controls and lung organoids, we found a proteoform that matched the MW of triphosphorylated and oxidized $\alpha 7$ (Figure S15A–C). The fact that this proteoform was found in HEK EBNA cells containing only i20S, and that a major increase in i20S upon activation of Caco2 cells with IFN γ was observed without changes in the relative abundance of mono vs. triphosphorylated $\alpha 7$, demonstrate that the presence of this proteoform does not correlate with the nature of the catalytic subunits. The two C-terminal serine residues (S243 and S250) were previously shown to be phosphorylated by protein kinase II [71] and have been confirmed in various proteomics and phosphoproteomics studies [69,70,72,73]. We here propose that the third phosphorylation might correspond to another site predicted on p.S142, as suggested by the NetPhos3.1 server. Early work from Castaño et al. [71], showed that deletion of the C-terminal part of $\alpha 7$ completely abolished the phosphorylation by protein kinase II, but has not been excluded that this third site might involve another kinase. In previous studies, triphosphorylated $\alpha 7$ has been reported in yeast, but two out of the three phosphosites were found on a protein segment that is absent in humans [49,55]. We found that one of these three phosphosites (probably S142) was particularly unstable upon freeze–thaw cycles, and even at 4 °C for a couple of hours, which may explain the absence of the phosphorylated residue in 20S from intestinal crypts (Figure S15D). The crypts were kept at -80 °C for several months after immunopurification, which might have caused the loss of the unstable phosphorylation. The 3rd phosphosite has not been detected in classical proteomics/phosphoproteomics approaches and immunoblotting

with phospho-specific antibodies that have long processing times and are thus prone to promote dephosphorylation of labile sites. We show here that the 3rd phosphorylation is completely lost in a couple of hours, which is compatible with our TD-MS workflow but not with overnight trypsin digestion (proteomics) or Western blot analysis. We will further investigate the function of this third phosphosite in the future, as phosphorylation of $\alpha 7$ was previously shown to regulate 26S stability [69] and Ecm29 binding [49]. Of note, any other PTM can be in theory identified by TD-MS, provided that it is stable in the gas phase, as we previously showed on the mycoloylation of porines from *Corinebacterium glutamicum* [84] or on the combined acylation and glycosylation of the LpqH antigen from *Mycobacterium tuberculosis* [85]. Concerning the ubiquitin proteasome system, detecting single or multiple O-GlcNAc [86–88], glutathionylation [89], ADP-ribosylation [90], succinylation [91] or myristoylation [92] could be of particular interest.

Our workflow combining TD-MS and BU-MS (Figure 8) allowed us to confirm mutations in BLCLs derived from PRAAS related patients and their parents and we provided further insights on the possible effect of these disease-causing mutations on 20S assembly. Our results confirmed that Patient A was homozygous for the p.(T75M) mutation in $\beta 5i$ and that this mutation mainly affected the chymotrypsin-like activity and only minimally decreased the incorporation and the binding of other molecules to the 20S. This is to be expected, as this mutation affects the third threonine from the catalytic triad of the $\beta 5i$ subunit conferring the chymotryptic-like activity. Previous modeling of this mutation predicted only a slight local structural rearrangement [18,27].

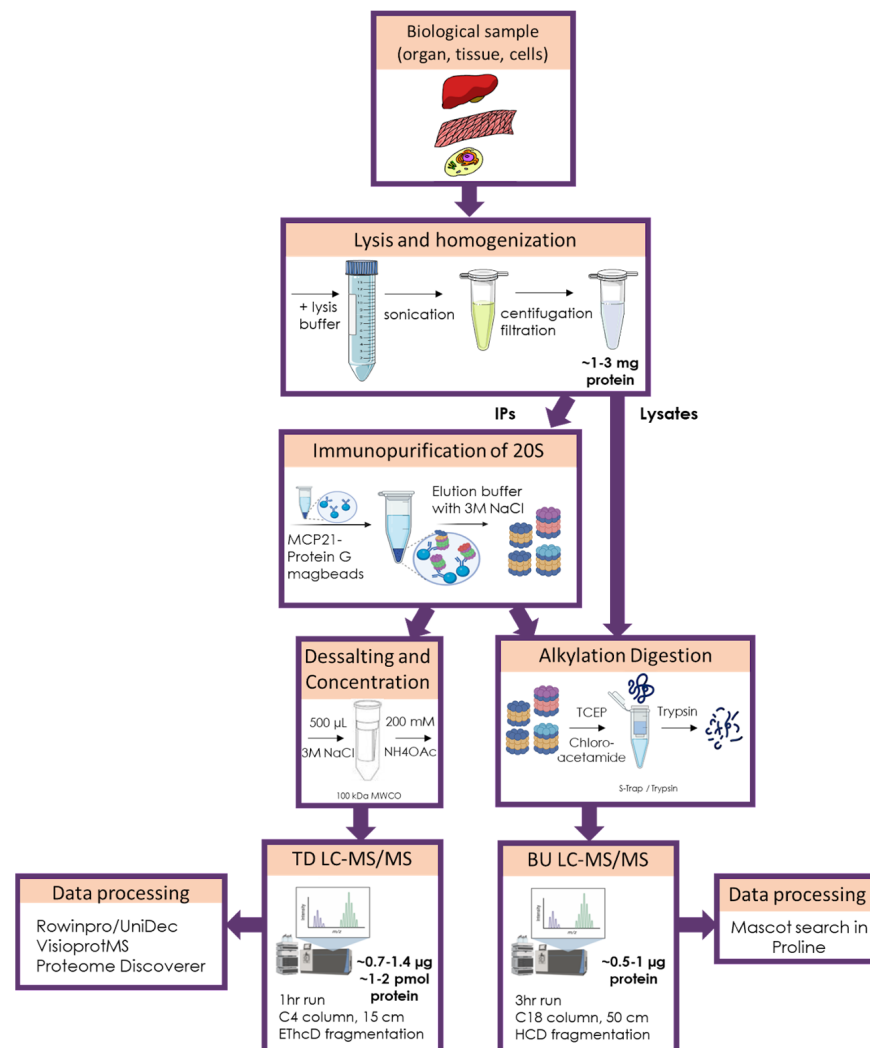


Figure 8. Workflow of our complementary TD-MS and BU-MS analysis of 20S proteasome complexes.

The proteoform footprint and the label-free TD-MS of the proteoforms of immunopurified 20S from Patient B showed very similar abundances of WT and p.(T75M) $\beta 5i$, but almost no incorporation of p.(R233del) $\alpha 7$, confirming in a single experiment that only the first mutated isoform can be found in fully assembled 20S complexes. Work from Brehm et al. had demonstrated that this patient had normal $\alpha 7$ mRNA levels but no protein expression, thus suggesting that the p.(R233del) mutation affects exclusively the $\alpha 7$ stability as it probably alters subunit folding [18]. Although label-free BU proteomics was not able to distinguish and thus quantify the WT and R233del isoforms of $\alpha 7$, contrary to our label-free TD quantification, BU analyses showed no changes in terms of 20S content in the lysates and assembling 20S in the immunopurified complex, respectively, confirming this finding. Moreover, since the caspase-like activity of 20S from Patient A (homozygous for p.(T75M) $\beta 5i$) and from a control harboring the p.(R60H) $\beta 1i$ SNP were not significantly affected, one can reasonably argue that the decrease in caspase-like activity observed in Patient B was solely due to this p.(R233del) in $\alpha 7$, even though synergistic effects between p.(R233del) $\alpha 7$ and p.(R60H) $\beta 1i$ cannot be excluded at this stage.

The effect of $\beta 7$ p.(D212_214del) was even more severe than the $\alpha 7$ p.(R233del) (4% incorporation) as it could not be detected at all in the immunopurified 20S proteoform footprint. This was expected, since, as described previously, $\beta 7$ is the last subunit being incorporated into the 20S before dimerization [93,94] and these three residues are located in a helix near its the C-terminal region, which has been reported to be essential for the dimerization step during assembly [18,78]. We could also confirm by TD-MSMS sequencing two SNPs that were also present in genetic analyses of the patients: p.(I234T) in $\beta 7$ in the father of Patient C and p.(R60H) in $\beta 1i$ of Patients A and B (homozygous), in the mother of Patient C (heterozygous) and in two healthy controls. While the p.(R60H) SNP is very common and not disease-related, the p.(I234T) variant has been predicted to be one of the SNPs that has significant genotypic association with depression [95].

These patient-derived BLCL were instrumental to optimize our pipeline before applying it to more rare and precious samples such as biopsies. They showed the complementarity of the information obtained by both TD and BU approaches, as well as their limitations.

We then investigated whether our TD-MS workflow was able to monitor the 20S immuno subunits after immunopurification of lysates of increasing complexity, i.e., cell lines, organoids, and biopsies. We found out that a starting quantity of 1–3 mg total protein was enough to successfully establish these 20S proteoform footprints, implying that this method can be used for precious biological samples such as disease-related biopsies.

We also investigated its potential application for intra-acquisition relative quantification of different subunits, in order to quickly establish the proportion of c20S and i20S in a sample. We confirmed that the ionization yields of the different α and β subunits were quite different (ranging from 30% to 160% relative to the average of all the non-catalytic subunits), but reproducible. This allowed us to semi-quantify the relative amount of catalytic subunits after induction of the i20S in Caco2 cells and also in lung organoids and colorectal crypts from patients. Even though the standard deviations were not negligible, the obtained values were in good agreement with the expected ratios (Figure S12), showing that this relative quantification with the correction of abundances with RIY using top-down MS can be used to determine the relative abundance of c20S vs. i20S proteasomes. Interestingly, $\beta 5$ and $\beta 5i$ both show good ionization yields compared to the other catalytic subunits, and since they are present in all the immuno subunit-containing proteasomes (i.e., even the intermediates); quantifying the relative signal of $\beta 5$ vs. $\beta 5i$ represents a fast and robust way of measuring the relative abundance of c20S vs. i20S, even for low-abundance sample in which the other catalytic subunits might not be detected.

5. Conclusions and Perspectives

The advantage of our workflow is threefold: it provides not only a relatively fast turnaround (approximately 2 h, including data analysis) but also a very thorough characterization of the different 20S proteoforms present in the sample; this is an aspect that

is often overlooked by other methods. Finally, this very sensitive method is compatible with valuable and low-abundance clinical samples to detect the expression of variants or SNPs. For example, we identified the presence of multiple phosphorylated forms of $\alpha 7$, whose function(s) and precise localization, however, still need to be investigated. On the other hand, even though the method still suffers from inaccuracy due to reproducibility issues in terms of ionization yields, it allowed us to provide a good estimate of the 20S composition. In terms of sensitivity, we were able to analyze immunopurified 20S starting from 10×10^6 Caco2 cells and from ~50,000 crypts, corresponding to ~1–3 mg of starting material in the lysate and ~1–2 pmol (0.7–1.4 μg) of 20S injected in the mass spectrometer; this is in good agreement with the quantity of total protein commonly injected on this instrument for shotgun BU experiments. The main bottleneck in terms of TD sensitivity compared to BU thus does not arise from the sensitivity of the mass spectrometer, but rather from its difficulty in analyzing complex mixtures (lysates), hence the need to immunopurify the 20S proteasome and start from higher quantity of material. However, the level of information obtained here is much higher, and we consider that the two approaches are complementary. Furthermore, as instruments are becoming not only more sensitive but also able to analyze more complex mixtures, we foresee that the use of TD proteomics will be exponential in the near future. For example, we expect that new developments such as proton charge transfer reduction [96] or charge detection mass spectrometry [97] combined with more efficient fragmentation techniques such as ultraviolet photodissociation [98], electron capture dissociation [99] or surface induced dissociation [100] will allow the analysis of higher MW and lower-abundance species. In the case of proteasome complexes, this will potentially expand our research to co-immunopurified regulators or proteasome interacting proteins, since other diseases are related to mutations of chaperone (PAC2, POMP) or 19S subunits [18,37,41].

Now that we have showed that the workflow can be used in tissues/biopsies from patients, we intend to apply it to other proteasome subtypes or in different pathological contexts, for example, to investigate the role of the i20S in different inflammatory bowel diseases from resections of patients. Finally, the determination of RIY for intra-acquisition/semi-quantification of protein complex subunits can be applied to any other multiprotein/multiproteoform complexes, including ribosomes and inflammasomes, to name but a few.

Supplementary Materials: Further details concerning the relative label-free quantification of c20S and i20S proteasomes and Supplementary Figures can be found in the Supplementary materials. The following are available online at <https://www.mdpi.com/article/10.3390/cells12060844/s1>. Figure S1: TD-MS identification of proteoforms in human immunoproteasome (i20S) purified from HEK-EBNA cells; Figure S2: Proteoform map of $\alpha 7$ from human immunoproteasome (i20S) purified from HEK-EBNA cells identified by TD-MS; Figure S3: Relative trypsin-like and caspase-like activities of Patient A, B and C and his parents compared to healthy controls; Figure S4: Bottom-up mass spectrometry (BU-MS) analysis of lysates and immunopurified 20S from PRAAS patients; Figure S5: MSMS top-down sequencing of the oxidized forms of T75M and WT $\beta 5i$ of 20S immunopurified from PRAAS Patient B ($\beta 5i$ T75M and $\alpha 7$ R233del); Figure S6: MSMS top-down sequencing of the oxidized form of I234T SNP $\beta 7$ of 20S; Figure S7: Characterization of $\beta 1i$ (PSMB9) proteoforms of immunopurified 20S from PRAAS patients by TD-MS; Figure S8: Proteoform maps from VisioprotMS of c20S and i20S purified from HEK-EBNA cells, and 50%:50% c20S:i20S mix analyzed by TD-MS; Figure S9: Averaged Relative Ionization Yields (relative to the average intensities of non-catalytic subunits) of each proteasome subunit in TD-MS; Figure S10: Comparison of relative ionization yields of 20S proteasome subunits in different buffers with different TD-MS acquisition methods; Figure S11: Titration of known c20S and i20S mixes analyzed by TD-MS; Figure S12: Experimental vs. expected i20S relative abundances obtained by TD-MS with normalization only and with RIY correction then normalization; Figure S13: Relative label-free quantification (LFQ) of immunopurified 20S from different samples, showing the benefit of applying the correction of abundances with the relative ionization yield (RIY) in TD-MS; Figure S14: Relative abundances of catalytic subunits obtained with

TD-MS; Figure S15: The highly unstable triply phosphorylated $\alpha 7$ proteoform found by TD-MS in samples containing both c20S and i20.

Author Contributions: All authors contributed to editing the manuscript and figures. A.S.D. and D.Ž. performed the experiments and data analysis. C.F. provided expertise on MS. S.A.L.-I., C.C. and E.M. expanded and provided the airway organoids. D.B., L.A., M.Q.-N. and A.F. provided the intestinal crypts. S.M. and F.E. expanded and provided the BLCLs; E.K., A.A.d.J. and R.G.-M. critical expertise on PRAAS-CANDLE mutations and E.K. expertise on i20S and i20S assembly. O.B.-S. provided critical expertise on the proteasome. J.M. and M.-P.B. designed, performed and supervised the experiments, data analysis, and wrote the paper with contribution from all the authors. All authors have read and agreed to the published version of the manuscript.

Funding: This work was supported by the French Ministry of Research (ANR-ProteasoRegMS to J.M., ANR-PA200_IN_IPF to M.-P.B. and Investissements d’Avenir Program, Proteomics French Infrastructure (ANR-10-INBS-08 to O.B.-S.), the Fonds Européens de Développement Régional Toulouse Métropole and the Région Midi-Pyrénées (O.B.-S.), the German Research Foundation (RTG 2719 PRO to S.M., F.E. and E.K.) and the Intramural Research Program of NIAID at the NIH (A.A.-J. and R.G.-M.).

Institutional Review Board Statement: All PRAAS patients were enrolled in the natural history protocol 17-I-0016/NCT02974595 that is approved by the NIAID and NIAMS/NIIDDK Institutional Review Boards (National Institutes of Health, Bethesda, MD).

Informed Consent Statement: (1) PRAAS patients: Written informed consent was obtained from the parents of all patients/healthy controls involved, and assent was obtained from the patients/healthy controls were indicated. All patients (A, B and C), the parents of Patient C and healthy controls 1 to 4 underwent genetic analyses including whole exome or genome sequencing and trio analysis at the NIH Clinical Center. (2) Intestinal crypts: Colon tissue samples were obtained from patients treated at the Toulouse University Hospital. Patients gave informed consent, and were included in the registered COLIC study (DC-2015-2443). (3) Airway Organoids: The CHU of Toulouse provided human lung biopsies of healthy adjacent tissue from lung cancer patients under the CNRS-approved protocol (CHU 19 244 C and Ref CNRS 205782).

Data Availability Statement: Data is available upon request.

Conflicts of Interest: The authors declare no conflict of interest.

References

1. Kasahara, M.; Flajnik, M.F. Origin and Evolution of the Specialized Forms of Proteasomes Involved in Antigen Presentation. *Immunogenetics* **2019**, *71*, 251–261. [[CrossRef](#)] [[PubMed](#)]
2. Guillaume, B.; Chapiro, J.; Stroobant, V.; Colau, D.; Van Holle, B.; Parvizi, G.; Bousquet-Dubouch, M.-P.; Théate, I.; Parmentier, N.; Van den Eynde, B.J. Two Abundant Proteasome Subtypes That Uniquely Process Some Antigens Presented by HLA Class I Molecules. *Proc. Natl. Acad. Sci. USA* **2010**, *107*, 18599–18604. [[CrossRef](#)] [[PubMed](#)]
3. Winter, M.B.; La Greca, F.; Arastu-Kapur, S.; Caiazza, F.; Cimermanic, P.; Buchholz, T.J.; Anderl, J.L.; Ravalin, M.; Bohn, M.F.; Sali, A.; et al. Immunoproteasome Functions Explained by Divergence in Cleavage Specificity and Regulation. *eLife* **2017**, *6*, e27364. [[CrossRef](#)]
4. Raule, M.; Cerruti, F.; Cascio, P. Enhanced Rate of Degradation of Basic Proteins by 26S Immunoproteasomes. *Biochim. Biophys. Acta BBA-Mol. Cell Res.* **2014**, *1843*, 1942–1947. [[CrossRef](#)]
5. Fabre, B.; Lambour, T.; Garrigues, L.; Amalric, F.; Vigneron, N.; Menneteau, T.; Stella, A.; Monsarrat, B.; Van den Eynde, B.; Burlet-Schiltz, O.; et al. Deciphering Preferential Interactions within Supramolecular Protein Complexes: The Proteasome Case. *Mol. Syst. Biol.* **2015**, *11*, 771. [[CrossRef](#)]
6. Kim, S.; Park, S.H.; Choi, W.H.; Lee, M.J. Evaluation of Immunoproteasome-Specific Proteolytic Activity Using Fluorogenic Peptide Substrates. *Immune Netw.* **2022**, *22*, e28. [[CrossRef](#)] [[PubMed](#)]
7. Basler, M.; Groettrup, M. On the Role of the Immunoproteasome in Protein Homeostasis. *Cells* **2021**, *10*, 3216. [[CrossRef](#)]
8. Lesne, J.; Bousquet, M.-P.; Marcoux, J.; Locard-Paulet, M. Top-Down and Intact Protein Mass Spectrometry Data Visualization for Proteoform Analysis Using VisioProt-MS. *Bioinform. Biol. Insights* **2019**, *13*, 1177932219868223. [[CrossRef](#)]
9. Živković, D.; Sanchez Dafun, A.; Menneteau, T.; Schahl, A.; Lise, S.; Kervarrec, C.; Toste Rêgo, A.; da Fonseca, P.C.A.; Chavent, M.; Pineau, C.; et al. Proteasome Complexes Experience Profound Structural and Functional Rearrangements throughout Mammalian Spermatogenesis. *Proc. Natl. Acad. Sci. USA* **2022**, *119*, e2116826119. [[CrossRef](#)]

10. Akiyama, K.; Kagawa, S.; Tamura, T.; Shimbara, N.; Takashina, M.; Kristensen, P.; Hendil, K.B.; Tanaka, K.; Ichihara, A. Replacement of Proteasome Subunits X and Y by LMP7 and LMP2 Induced by Interferon-Gamma for Acquisition of the Functional Diversity Responsible for Antigen Processing. *FEBS Lett.* **1994**, *343*, 85–88. [[CrossRef](#)]
11. Khan, S.; van den Broek, M.; Schwarz, K.; de Giuli, R.; Diener, P.-A.; Groettrup, M. Immunoproteasomes Largely Replace Constitutive Proteasomes During an Antiviral and Antibacterial Immune Response in the Liver. *J. Immunol.* **2001**, *167*, 6859–6868. [[CrossRef](#)] [[PubMed](#)]
12. Kincaid, E.Z.; Che, J.W.; York, I.; Escobar, H.; Reyes-Vargas, E.; Delgado, J.C.; Welsh, R.M.; Karow, M.L.; Murphy, A.J.; Valenzuela, D.M.; et al. Mice Completely Lacking Immunoproteasomes Show Major Changes in Antigen Presentation. *Nat. Immunol.* **2011**, *13*, 129–135. [[CrossRef](#)]
13. Moebius, J.; van den Broek, M.; Groettrup, M.; Basler, M. Immunoproteasomes Are Essential for Survival and Expansion of T Cells in Virus-Infected Mice. *Eur. J. Immunol.* **2010**, *40*, 3439–3449. [[CrossRef](#)]
14. Abi Habib, J.; De Plaen, E.; Stroobant, V.; Zivkovic, D.; Bousquet, M.-P.; Guillaume, B.; Wahni, K.; Messens, J.; Busse, A.; Vigneron, N.; et al. Efficiency of the Four Proteasome Subtypes to Degrade Ubiquitinated or Oxidized Proteins. *Sci. Rep.* **2020**, *10*, 15765. [[CrossRef](#)]
15. Menneteau, T.; Fabre, B.; Garrigues, L.; Stella, A.; Zivkovic, D.; Roux-Dalvai, F.; Mouton-Barbosa, E.; Beau, M.; Renoud, M.-L.; Amalric, F.; et al. Mass Spectrometry-Based Absolute Quantification of 20S Proteasome Status for Controlled Ex-Vivo Expansion of Human Adipose-Derived Mesenchymal Stromal/Stem Cells. *Mol. Cell. Proteomics MCP* **2019**, *18*, 744–759. [[CrossRef](#)] [[PubMed](#)]
16. Pickering, A.M.; Koop, A.L.; Teoh, C.Y.; Ermak, G.; Grune, T.; Davies, K.J.A. The Immunoproteasome, the 20S Proteasome, and the PA28 $\alpha\beta$ Proteasome Regulator are Oxidative-Stress-Adaptive Proteolytic Complexes. *Biochem. J.* **2010**, *432*, 585–594. [[CrossRef](#)]
17. Seifert, U.; Bialy, L.P.; Ebstein, F.; Bech-Otschir, D.; Voigt, A.; Schröter, F.; Prozorovski, T.; Lange, N.; Steffen, J.; Rieger, M.; et al. Immunoproteasomes Preserve Protein Homeostasis upon Interferon-Induced Oxidative Stress. *Cell* **2010**, *142*, 613–624. [[CrossRef](#)] [[PubMed](#)]
18. Brehm, A.; Liu, Y.; Sheikh, A.; Marrero, B.; Omoyinmi, E.; Zhou, Q.; Montealegre, G.; Biancotto, A.; Reinhardt, A.; de Jesus, A.A.; et al. Additive Loss-of-Function Proteasome Subunit Mutations in CANDLER/PRAAS Patients Promote Type I IFN Production. *J. Clin. Investig.* **2015**, *125*, 4196–4211. [[CrossRef](#)]
19. Davidson, S.; Yu, C.-H.; Steiner, A.; Ebstein, F.; Baker, P.J.; Jarur-Chamy, V.; Hrovat Schaale, K.; Laohamonthonkul, P.; Kong, K.; Calleja, D.J.; et al. Protein Kinase R Is an Innate Immune Sensor of Proteotoxic Stress via Accumulation of Cytoplasmic IL-24. *Sci. Immunol.* **2022**, *7*, eabi6763. [[CrossRef](#)]
20. Çetin, G.; Studencka-Turski, M.; Venz, S.; Schormann, E.; Junker, H.; Hammer, E.; Völker, U.; Ebstein, F.; Krüger, E. Immunoproteasomes Control Activation of Innate Immune Signaling and Microglial Function. *Front. Immunol.* **2022**, *13*. [[CrossRef](#)]
21. Kors, S.; Geijtenbeek, K.; Reits, E.; Schipper-Krom, S. Regulation of Proteasome Activity by (Post-)Transcriptional Mechanisms. *Front. Mol. Biosci.* **2019**, *6*, 48. [[CrossRef](#)] [[PubMed](#)]
22. Guo, X.; Huang, X.; Chen, M.J. Reversible Phosphorylation of the 26S Proteasome. *Protein Cell* **2017**, *8*, 255–272. [[CrossRef](#)]
23. Gomes, A.V. Genetics of Proteasome Diseases. *Scientifica* **2013**, *2013*, 637629. [[CrossRef](#)] [[PubMed](#)]
24. Fernández-Cruz, I.; Reynaud, E. Proteasome Subunits Involved in Neurodegenerative Diseases. *Arch. Med. Res.* **2021**, *52*, 1–14. [[CrossRef](#)] [[PubMed](#)]
25. Coux, O.; Zieba, B.A.; Meiners, S. The Proteasome System in Health and Disease. In *Proteostasis and Disease: From Basic Mechanisms to Clinics*; Barrio, R., Sutherland, J.D., Rodriguez, M.S., Eds.; Springer International Publishing: Cham, Switzerland, 2020; pp. 55–100. ISBN 9783030382667.
26. Goetzke, C.C.; Ebstein, F.; Kallinich, T. Role of Proteasomes in Inflammation. *J. Clin. Med.* **2021**, *10*, 1783. [[CrossRef](#)] [[PubMed](#)]
27. Agarwal, A.K.; Xing, C.; DeMartino, G.N.; Mizrachi, D.; Hernandez, M.D.; Sousa, A.B.; Martínez de Villarreal, L.; dos Santos, H.G.; Garg, A. PSMB8 Encoding the B5i Proteasome Subunit Is Mutated in Joint Contractures, Muscle Atrophy, Microcytic Anemia, and Panniculitis-Induced Lipodystrophy Syndrome. *Am. J. Hum. Genet.* **2010**, *87*, 866–872. [[CrossRef](#)]
28. Arima, K.; Kinoshita, A.; Mishima, H.; Kanazawa, N.; Kaneko, T.; Mizushima, T.; Ichinose, K.; Nakamura, H.; Tsujino, A.; Kawakami, A.; et al. Proteasome Assembly Defect Due to a Proteasome Subunit Beta Type 8 (PSMB8) Mutation Causes the Autoinflammatory Disorder, Nakajo-Nishimura Syndrome. *Proc. Natl. Acad. Sci. USA* **2011**, *108*, 14914–14919. [[CrossRef](#)]
29. Kitamura, A.; Maekawa, Y.; Uehara, H.; Izumi, K.; Kawachi, I.; Nishizawa, M.; Toyoshima, Y.; Takahashi, H.; Standley, D.M.; Tanaka, K.; et al. A Mutation in the Immunoproteasome Subunit PSMB8 Causes Autoinflammation and Lipodystrophy in Humans. *J. Clin. Investig.* **2011**, *121*, 4150–4160. [[CrossRef](#)]
30. Liu, Y.; Ramot, Y.; Torrelo, A.; Paller, A.S.; Si, N.; Babay, S.; Kim, P.W.; Sheikh, A.; Lee, C.-C.R.; Chen, Y.; et al. Mutations in Proteasome Subunit β Type 8 Cause Chronic Atypical Neutrophilic Dermatitis with Lipodystrophy and Elevated Temperature with Evidence of Genetic and Phenotypic Heterogeneity. *Arthritis Rheum.* **2012**, *64*, 895–907. [[CrossRef](#)]
31. Kluk, J.; Rustin, M.; Brogan, P.A.; Omoyinmi, E.; Rowczenio, D.M.; Wilcocks, L.C.; Melly, L.; Lachmann, H.J. Chronic Atypical Neutrophilic Dermatitis with Lipodystrophy and Elevated Temperature Syndrome: A Report of a Novel Mutation and Review of the Literature. *Br. J. Dermatol.* **2014**, *170*, 215–217. [[CrossRef](#)]
32. Cavalcante, M.P.V.; Brunelli, J.B.; Miranda, C.C.; Novak, G.V.; Malle, L.; Aikawa, N.E.; Jesus, A.A.; Silva, C.A. CANDLER Syndrome: Chronic Atypical Neutrophilic Dermatitis with Lipodystrophy and Elevated Temperature—a Rare Case with a Novel Mutation. *Eur. J. Pediatr.* **2016**, *175*, 735–740. [[CrossRef](#)]

33. Tüfekçi, Ö.; Bengoa, S.; Karapinar, T.H.; Ataseven, E.B.; Irken, G.; Ören, H. CANDLE Syndrome: A Recently Described Autoinflammatory Syndrome. *J. Pediatr. Hematol. Oncol.* **2015**, *37*, 296–299. [[CrossRef](#)]
34. Kanazawa, N.; Hemmi, H.; Kinjo, N.; Ohnishi, H.; Hamazaki, J.; Mishima, H.; Kinoshita, A.; Mizushima, T.; Hamada, S.; Hamada, K.; et al. Heterozygous Missense Variant of the Proteasome Subunit β -Type 9 Causes Neonatal-Onset Autoinflammation and Immunodeficiency. *Nat. Commun.* **2021**, *12*, 6819. [[CrossRef](#)] [[PubMed](#)]
35. Sarabay, G.; Méchin, D.; Salhi, A.; Boursier, G.; Rittore, C.; Crow, Y.; Rice, G.; Tran, T.-A.; Cezar, R.; Duffy, D.; et al. PSMB10, the Last Immunoproteasome Gene Missing for PRAAS. *J. Allergy Clin. Immunol.* **2020**, *145*, 1015–1017.e6. [[CrossRef](#)] [[PubMed](#)]
36. Verhoeven, D.; Schonenberg-Meinema, D.; Ebstein, F.; Papendorf, J.J.; Baars, P.A.; van Leeuwen, E.M.M.; Jansen, M.H.; Lankester, A.C.; van der Burg, M.; Florquin, S.; et al. Hematopoietic Stem Cell Transplantation in a Patient with Proteasome-Associated Autoinflammatory Syndrome (PRAAS). *J. Allergy Clin. Immunol.* **2022**, *149*, 1120–1127.e8. [[CrossRef](#)] [[PubMed](#)]
37. De Jesus, A.A.; Brehm, A.; VanTries, R.; Pillet, P.; Parentelli, A.-S.; Montealegre Sanchez, G.A.; Deng, Z.; Paut, I.K.; Goldbach-Mansky, R.; Krüger, E. Novel Proteasome Assembly Chaperone Mutations in PSMG2/PAC2, Cause the Autoinflammatory Interferonopathy, CANDLE/PRAAS4. *J. Allergy Clin. Immunol.* **2019**, *143*, 1939–1943.e8. [[CrossRef](#)] [[PubMed](#)]
38. Poli, M.C.; Ebstein, F.; Nicholas, S.K.; de Guzman, M.M.; Forbes, L.R.; Chinn, I.K.; Mace, E.M.; Vogel, T.P.; Carisey, A.F.; Benavides, F.; et al. Heterozygous Truncating Variants in POMP Escape Nonsense-Mediated Decay and Cause a Unique Immune Dysregulatory Syndrome. *Am. J. Hum. Genet.* **2018**, *102*, 1126–1142. [[CrossRef](#)]
39. Küry, S.; Besnard, T.; Ebstein, F.; Khan, T.N.; Gambin, T.; Douglas, J.; Bacino, C.A.; Craigen, W.J.; Sanders, S.J.; Lehmann, A.; et al. De Novo Disruption of the Proteasome Regulatory Subunit PSMD12 Causes a Syndromic Neurodevelopmental Disorder. *Am. J. Hum. Genet.* **2017**, *100*, 352–363. [[CrossRef](#)]
40. Isidor, B.; Ebstein, F.; Hurst, A.; Vincent, M.; Bader, I.; Rudy, N.L.; Cogne, B.; Mayr, J.; Brehm, A.; Bupp, C.; et al. Stankiewicz-Isidor Syndrome: Expanding the Clinical and Molecular Phenotype. *Genet. Med. Off. J. Am. Coll. Med. Genet.* **2022**, *24*, 179–191. [[CrossRef](#)]
41. Kröll-Hermi, A.; Ebstein, F.; Stoetzel, C.; Geoffroy, V.; Schaefer, E.; Scheidecker, S.; Bär, S.; Takamiya, M.; Kawakami, K.; Zieba, B.A.; et al. Proteasome Subunit PSMC3 Variants Cause Neurosensory Syndrome Combining Deafness and Cataract Due to Proteotoxic Stress. *EMBO Mol. Med.* **2020**, *12*, e11861. [[CrossRef](#)]
42. Bonvini, P.; Zorzi, E.; Basso, G.; Rosolen, A. Bortezomib-Mediated 26S Proteasome Inhibition Causes Cell-Cycle Arrest and Induces Apoptosis in CD-30⁺ Anaplastic Large Cell Lymphoma. *Leukemia* **2007**, *21*, 838–842. [[CrossRef](#)] [[PubMed](#)]
43. Kuhn, D.J.; Chen, Q.; Voorhees, P.M.; Strader, J.S.; Shenk, K.D.; Sun, C.M.; Demo, S.D.; Bennett, M.K.; van Leeuwen, F.W.B.; Chanan-Khan, A.A.; et al. Potent Activity of Carfilzomib, a Novel, Irreversible Inhibitor of the Ubiquitin-Proteasome Pathway, against Preclinical Models of Multiple Myeloma. *Blood* **2007**, *110*, 3281–3290. [[CrossRef](#)] [[PubMed](#)]
44. Kupperman, E.; Lee, E.C.; Cao, Y.; Bannerman, B.; Fitzgerald, M.; Berger, A.; Yu, J.; Yang, Y.; Hales, P.; Bruzzese, F.; et al. Evaluation of the Proteasome Inhibitor MLN9708 in Preclinical Models of Human Cancer. *Cancer Res.* **2010**, *70*, 1970–1980. [[CrossRef](#)]
45. Basler, M.; Groettrup, M. Recent Insights How Combined Inhibition of Immuno/Proteasome Subunits Enables Therapeutic Efficacy. *Genes Immun.* **2020**, *21*, 273–287. [[CrossRef](#)]
46. Li, J.; Basler, M.; Alvarez, G.; Brunner, T.; Kirk, C.J.; Groettrup, M. Immunoproteasome Inhibition Prevents Chronic Antibody-Mediated Allograft Rejection in Renal Transplantation. *Kidney Int.* **2018**, *93*, 670–680. [[CrossRef](#)] [[PubMed](#)]
47. Koerner, J.; Brunner, T.; Groettrup, M. Inhibition and Deficiency of the Immunoproteasome Subunit LMP7 Suppress the Development and Progression of Colorectal Carcinoma in Mice. *Oncotarget* **2017**, *8*, 50873–50888. [[CrossRef](#)] [[PubMed](#)]
48. Basler, M.; Christ, M.; Goebel, H.; Groettrup, M. Immunoproteasome Upregulation Is Not Required to Control Protein Homeostasis during Viral Infection. *J. Immunol.* **2021**, *206*, 1697–1708. [[CrossRef](#)]
49. Wani, P.S.; Suppahia, A.; Capalla, X.; Ondracek, A.; Roelofs, J. Phosphorylation of the C-Terminal Tail of Proteasome Subunit A7 Is Required for Binding of the Proteasome Quality Control Factor Ecm29. *Sci. Rep.* **2016**, *6*, 27873. [[CrossRef](#)]
50. Froment, C.; Uttenweiler-Joseph, S.; Bousquet-Dubouch, M.-P.; Matondo, M.; Borges, J.-P.; Esmenjaud, C.; Lacroix, C.; Monsarrat, B.; Burlet-Schiltz, O. A Quantitative Proteomic Approach Using Two-Dimensional Gel Electrophoresis and Isotope-Coded Affinity Tag Labeling for Studying Human 20S Proteasome Heterogeneity. *Proteomics* **2005**, *5*, 2351–2363. [[CrossRef](#)]
51. Fabre, B.; Lambour, T.; Garrigues, L.; Ducoux-Petit, M.; Amalric, F.; Monsarrat, B.; Burlet-Schiltz, O.; Bousquet-Dubouch, M.-P. Label-Free Quantitative Proteomics Reveals the Dynamics of Proteasome Complexes Composition and Stoichiometry in a Wide Range of Human Cell Lines. *J. Proteome Res.* **2014**, *13*, 3027–3037. [[CrossRef](#)]
52. Fabre, B.; Lambour, T.; Delobel, J.; Amalric, F.; Monsarrat, B.; Burlet-Schiltz, O.; Bousquet-Dubouch, M.-P. Subcellular Distribution and Dynamics of Active Proteasome Complexes Unraveled by a Workflow Combining in Vivo Complex Cross-Linking and Quantitative Proteomics. *Mol. Cell. Proteomics MCP* **2013**, *12*, 687–699. [[CrossRef](#)]
53. Smith, L.M.; Kelleher, N.L.; Consortium for Top Down Proteomics. Proteoform: A Single Term Describing Protein Complexity. *Nat. Methods* **2013**, *10*, 186–187. [[CrossRef](#)]
54. Durbin, K.R.; Fornelli, L.; Fellers, R.T.; Doubleday, P.F.; Narita, M.; Kelleher, N.L. Quantitation and Identification of Thousands of Human Proteoforms below 30 KDa. *J. Proteome Res.* **2016**, *15*, 976–982. [[CrossRef](#)] [[PubMed](#)]
55. Gersch, M.; Hackl, M.W.; Dubiella, C.; Dobrinevski, A.; Groll, M.; Sieber, S.A. A Mass Spectrometry Platform for a Streamlined Investigation of Proteasome Integrity, Posttranslational Modifications, and Inhibitor Binding. *Chem. Biol.* **2015**, *22*, 404–411. [[CrossRef](#)] [[PubMed](#)]
56. Cupp-Sutton, K.A.; Wu, S. High-Throughput Quantitative Top-down Proteomics. *Mol. Omics* **2020**, *16*, 91–99. [[CrossRef](#)]

57. Collier, T.S.; Sarkar, P.; Rao, B.; Muddiman, D.C. Quantitative Top-down Proteomics of SILAC Labeled Human Embryonic Stem Cells. *J. Am. Soc. Mass Spectrom.* **2010**, *21*, 879–889. [[CrossRef](#)]
58. Winkels, K.; Koudelka, T.; Tholey, A. Quantitative Top-Down Proteomics by Isobaric Labeling with Thiol-Directed Tandem Mass Tags. *J. Proteome Res.* **2021**, *20*, 4495–4506. [[CrossRef](#)]
59. Yu, D.; Wang, Z.; Cupp-Sutton, K.A.; Guo, Y.; Kou, Q.; Smith, K.; Liu, X.; Wu, S. Quantitative Top-Down Proteomics in Complex Samples Using Protein-Level Tandem Mass Tag Labeling. *J. Am. Soc. Mass Spectrom.* **2021**, *32*, 1336–1344. [[CrossRef](#)] [[PubMed](#)]
60. Chen, Y.; Mao, P.; Wang, D. Quantitation of Intact Proteins in Human Plasma Using Top-Down Parallel Reaction Monitoring-MS. *Anal. Chem.* **2018**, *90*, 10650–10653. [[CrossRef](#)]
61. Ntai, I.; Toby, T.K.; LeDuc, R.D.; Kelleher, N.L. A Method for Label-Free, Differential Top-Down Proteomics. *Methods Mol. Biol.* **2016**, *1410*, 121–133. [[CrossRef](#)]
62. Geis-Asteggiante, L.; Ostrand-Rosenberg, S.; Fenselau, C.; Edwards, N.J. Evaluation of Spectral Counting for Relative Quantitation of Proteoforms in Top-Down Proteomics. *Anal. Chem.* **2016**, *88*, 10900–10907. [[CrossRef](#)] [[PubMed](#)]
63. Iakobachvili, N.; Leon-Icaza, S.A.; Knoops, K.; Sachs, N.; Mazères, S.; Simeone, R.; Peixoto, A.; Bernard, C.; Murriss-Espin, M.; Mazières, J.; et al. Mycobacteria–Host Interactions in Human Bronchiolar Airway Organoids. *Mol. Microbiol.* **2022**, *117*, 682–692. [[CrossRef](#)]
64. Sachs, N.; Papaspyropoulos, A.; Zomer-van Ommen, D.D.; Heo, I.; Böttinger, L.; Klay, D.; Weeber, F.; Huelsz-Prince, G.; Iakobachvili, N.; Amatngalim, G.D.; et al. Long-term Expanding Human Airway Organoids for Disease Modeling. *EMBO J.* **2019**, *38*, e100300. [[CrossRef](#)] [[PubMed](#)]
65. Bousquet-Dubouch, M.-P.; Baudelet, E.; Guérin, F.; Matondo, M.; Uttenweiler-Joseph, S.; Burlet-Schiltz, O.; Monsarrat, B. Affinity Purification Strategy to Capture Human Endogenous Proteasome Complexes Diversity and to Identify Proteasome-Interacting Proteins. *Mol. Cell. Proteomics* **2009**, *8*, 1150–1164. [[CrossRef](#)]
66. Locard-Paulet, M.; Parra, J.; Albigot, R.; Mouton-Barbosa, E.; Bardi, L.; Burlet-Schiltz, O.; Marcoux, J. VisioProt-MS: Interactive 2D Maps from Intact Protein Mass Spectrometry. *Bioinformatics* **2019**, *35*, 679–681. [[CrossRef](#)]
67. Marty, M.T.; Baldwin, A.J.; Marklund, E.G.; Hochberg, G.K.A.; Benesch, J.L.P.; Robinson, C.V. Bayesian Deconvolution of Mass and Ion Mobility Spectra: From Binary Interactions to Polydisperse Ensembles. *Anal. Chem.* **2015**, *87*, 4370–4376. [[CrossRef](#)] [[PubMed](#)]
68. Bouyssié, D.; Hesse, A.-M.; Mouton-Barbosa, E.; Rompais, M.; Macron, C.; Carapito, C.; Gonzalez de Peredo, A.; Couté, Y.; Dupierris, V.; Burel, A.; et al. Proline: An Efficient and User-Friendly Software Suite for Large-Scale Proteomics. *Bioinformatics* **2020**, *36*, 3148–3155. [[CrossRef](#)]
69. Bose, S.; Stratford, F.L.L.; Broadfoot, K.I.; Mason, G.G.F.; Rivett, A.J. Phosphorylation of 20S Proteasome Alpha Subunit C8 (Alpha7) Stabilizes the 26S Proteasome and Plays a Role in the Regulation of Proteasome Complexes by Gamma-Interferon. *Biochem. J.* **2004**, *378*, 177–184. [[CrossRef](#)]
70. Schmidt, F.; Dahlmann, B.; Hustoft, H.K.; Koehler, C.J.; Strozynski, M.; Kloß, A.; Zimny-Arndt, U.; Jungblut, P.R.; Thiede, B. Quantitative Proteome Analysis of the 20S Proteasome of Apoptotic Jurkat T Cells. *Amino Acids* **2011**, *41*, 351–361. [[CrossRef](#)]
71. Castaño, J.G.; Mahillo, E.; Arizti, P.; Arribas, J. Phosphorylation of C8 and C9 Subunits of the Multicatalytic Proteinase by Casein Kinase II and Identification of the C8 Phosphorylation Sites by Direct Mutagenesis. *Biochemistry* **1996**, *35*, 3782–3789. [[CrossRef](#)]
72. Mason, G.G.F.; Murray, R.Z.; Pappin, D.; Rivett, A.J. Phosphorylation of ATPase Subunits of the 26S Proteasome. *FEBS Lett.* **1998**, *430*, 269–274. [[CrossRef](#)] [[PubMed](#)]
73. Wang, X.; Chen, C.-F.; Baker, P.R.; Chen, P.; Kaiser, P.; Huang, L. Mass Spectrometric Characterization of the Affinity-Purified Human 26S Proteasome Complex. *Biochemistry* **2007**, *46*, 3553–3565. [[CrossRef](#)] [[PubMed](#)]
74. Zhou, H.; Di Palma, S.; Preisinger, C.; Peng, M.; Polat, A.N.; Heck, A.J.R.; Mohammed, S. Toward a Comprehensive Characterization of a Human Cancer Cell Phosphoproteome. *J. Proteome Res.* **2013**, *12*, 260–271. [[CrossRef](#)] [[PubMed](#)]
75. Blom, N.; Gammeltoft, S.; Brunak, S. Sequence and Structure-Based Prediction of Eukaryotic Protein Phosphorylation Sites. *J. Mol. Biol.* **1999**, *294*, 1351–1362. [[CrossRef](#)]
76. Blom, N.; Sicheritz-Pontén, T.; Gupta, R.; Gammeltoft, S.; Brunak, S. Prediction of Post-Translational Glycosylation and Phosphorylation of Proteins from the Amino Acid Sequence. *Proteomics* **2004**, *4*, 1633–1649. [[CrossRef](#)]
77. Claverol, S.; Burlet-Schiltz, O.; Girbal-Neuhauser, E.; Gairin, J.E.; Monsarrat, B. Mapping and Structural Dissection of Human 20 S Proteasome Using Proteomic Approaches. *Mol. Cell. Proteomics* **2002**, *1*, 567–578. [[CrossRef](#)]
78. Ramos, P.C.; Marques, A.J.; London, M.K.; Dohmen, R.J. Role of C-Terminal Extensions of Subunits B2 and B7 in Assembly and Activity of Eukaryotic Proteasomes*. *J. Biol. Chem.* **2004**, *279*, 14323–14330. [[CrossRef](#)]
79. Schwanhäusser, B.; Busse, D.; Li, N.; Dittmar, G.; Schuchhardt, J.; Wolf, J.; Chen, W.; Selbach, M. Global Quantification of Mammalian Gene Expression Control. *Nature* **2011**, *473*, 337–342. [[CrossRef](#)]
80. Visekruna, A.; Joeris, T.; Seidel, D.; Kroesen, A.; Lodenkemper, C.; Zeitz, M.; Kaufmann, S.H.E.; Schmidt-Ullrich, R.; Steinhoff, U. Proteasome-Mediated Degradation of IκBα and Processing of P105 in Crohn Disease and Ulcerative Colitis. *J. Clin. Investig.* **2006**, *116*, 3195–3203. [[CrossRef](#)]
81. Keller, I.E.; Vasyka, O.; Takenaka, S.; Kloß, A.; Dahlmann, B.; Willems, L.I.; Verdoes, M.; Overkleeft, H.S.; Marcos, E.; Adnot, S.; et al. Regulation of Immunoproteasome Function in the Lung. *Sci. Rep.* **2015**, *5*, 10230. [[CrossRef](#)]
82. Kimura, H.; Caturegli, P.; Takahashi, M.; Suzuki, K. New Insights into the Function of the Immunoproteasome in Immune and Nonimmune Cells. *J. Immunol. Res.* **2015**, *2015*, e541984. [[CrossRef](#)] [[PubMed](#)]

83. Wang, X.; Kammerl, I.; Eickelberg, O.; Schamberger, A.; Meiners, S. Role of the Immunoproteasome during of Bronchial Epithelial Cell Differentiation. *ERJ Open Res.* **2019**, *5*. [[CrossRef](#)]
84. Carel, C.; Marcoux, J.; Réat, V.; Parra, J.; Latgé, G.; Laval, F.; Demange, P.; Burlet-Schiltz, O.; Milon, A.; Daffé, M.; et al. Identification of Specific Posttranslational O-Mycoloylations Mediating Protein Targeting to the Mycomembrane. *Proc. Natl. Acad. Sci. USA* **2017**, *114*, 4231–4236. [[CrossRef](#)] [[PubMed](#)]
85. Parra, J.; Marcoux, J.; Poncin, I.; Canaan, S.; Herrmann, J.L.; Nigou, J.; Burlet-Schiltz, O.; Rivière, M. Scrutiny of Mycobacterium Tuberculosis 19 KDa Antigen Proteoforms Provides New Insights in the Lipoglycoprotein Biogenesis Paradigm. *Sci. Rep.* **2017**, *7*, 43682. [[CrossRef](#)]
86. Zhang, F.; Su, K.; Yang, X.; Bowe, D.B.; Paterson, A.J.; Kudlow, J.E. O-GlcNAc Modification Is an Endogenous Inhibitor of the Proteasome. *Cell* **2003**, *115*, 715–725. [[CrossRef](#)]
87. Xu, J.; Wang, S.; Viollet, B.; Zou, M.-H. Regulation of the Proteasome by AMPK in Endothelial Cells: The Role of O-GlcNAc Transferase (OGT). *PLOS ONE* **2012**, *7*, e36717. [[CrossRef](#)]
88. Pecori, F.; Kondo, N.; Ogura, C.; Miura, T.; Kume, M.; Minamijima, Y.; Yamamoto, K.; Nishihara, S. Site-Specific O-GlcNAcylation of Psme3 Maintains Mouse Stem Cell Pluripotency by Impairing P-Body Homeostasis. *Cell Rep.* **2021**, *36*, 109361. [[CrossRef](#)] [[PubMed](#)]
89. Demasi, M.; Silva, G.M.; Netto, L.E.S. 20 S Proteasome from *Saccharomyces Cerevisiae* Is Responsive to Redox Modifications and Is S-Glutathionylated. *J. Biol. Chem.* **2003**, *278*, 679–685. [[CrossRef](#)]
90. Cho-Park, P.F.; Steller, H. Proteasome Regulation by ADP-Ribosylation. *Cell* **2013**, *153*, 614–627. [[CrossRef](#)]
91. Tsimokha, A.S.; Artamonova, T.O.; Diakonov, E.E.; Khodorkovskii, M.A.; Tomilin, A.N. Post-Translational Modifications of Extracellular Proteasome. *Molecules* **2020**, *25*, 3504. [[CrossRef](#)]
92. Kimura, A.; Kato, Y.; Hirano, H. N-Myristoylation of the Rpt2 Subunit Regulates Intracellular Localization of the Yeast 26S Proteasome. *Biochemistry* **2012**, *51*, 8856–8866. [[CrossRef](#)]
93. Bai, M.; Zhao, X.; Sahara, K.; Ohte, Y.; Hirano, Y.; Kaneko, T.; Yashiroda, H.; Murata, S. Assembly Mechanisms of Specialized Core Particles of the Proteasome. *Biomolecules* **2014**, *4*, 662–677. [[CrossRef](#)] [[PubMed](#)]
94. Hirano, Y.; Kaneko, T.; Okamoto, K.; Bai, M.; Yashiroda, H.; Furuyama, K.; Kato, K.; Tanaka, K.; Murata, S. Dissecting β -Ring Assembly Pathway of the Mammalian 20S Proteasome. *EMBO J.* **2008**, *27*, 2204–2213. [[CrossRef](#)] [[PubMed](#)]
95. Wong, M.-L.; Dong, C.; Andreev, V.; Arcos-Burgos, M.; Licinio, J. Prediction of Susceptibility to Major Depression by a Model of Interactions of Multiple Functional Genetic Variants and Environmental Factors. *Mol. Psychiatry* **2012**, *17*, 624–633. [[CrossRef](#)]
96. Huguet, R.; Mullen, C.; Srzentić, K.; Greer, J.B.; Fellers, R.T.; Zabrouskov, V.; Syka, J.E.P.; Kelleher, N.L.; Fornelli, L. Proton Transfer Charge Reduction Enables High-Throughput Top-Down Analysis of Large Proteoforms. *Anal. Chem.* **2019**, *91*, 15732–15739. [[CrossRef](#)] [[PubMed](#)]
97. Kafader, J.O.; Durbin, K.R.; Melani, R.D.; Des Soye, B.J.; Schachner, L.F.; Senko, M.W.; Compton, P.D.; Kelleher, N.L. Individual Ion Mass Spectrometry Enhances the Sensitivity and Sequence Coverage of Top-Down Mass Spectrometry. *J. Proteome Res.* **2020**, *19*, 1346–1350. [[CrossRef](#)] [[PubMed](#)]
98. Blevins, M.S.; Juetten, K.J.; James, V.K.; Butalewicz, J.P.; Escobar, E.E.; Lanzillotti, M.B.; Sanders, J.D.; Fort, K.L.; Brodbelt, J.S. Nanohydrophobic Interaction Chromatography Coupled to Ultraviolet Photodissociation Mass Spectrometry for the Analysis of Intact Proteins in Low Charge States. *J. Proteome Res.* **2022**, *21*, 2493–2503. [[CrossRef](#)]
99. Greisch, J.-F.; den Boer, M.A.; Lai, S.-H.; Gallagher, K.; Bondt, A.; Commandeur, J.; Heck, A.J.R. Extending Native Top-Down Electron Capture Dissociation to MDa Immunoglobulin Complexes Provides Useful Sequence Tags Covering Their Critical Variable Complementarity-Determining Regions. *Anal. Chem.* **2021**, *93*, 16068–16075. [[CrossRef](#)]
100. Harvey, S.R.; Ben-Nissan, G.; Sharon, M.; Wysocki, V.H. Surface-Induced Dissociation for Protein Complex Characterization. *Methods Mol. Biol. Clifton NJ* **2022**, *2500*, 211–237. [[CrossRef](#)]

Disclaimer/Publisher's Note: The statements, opinions and data contained in all publications are solely those of the individual author(s) and contributor(s) and not of MDPI and/or the editor(s). MDPI and/or the editor(s) disclaim responsibility for any injury to people or property resulting from any ideas, methods, instructions or products referred to in the content.